

Combined CO & Dust Scaling Relations of Depletion Time and Molecular Gas Fractions with Cosmic Time, Specific Star Formation Rate and Stellar Mass¹

R.Genzel^{1,2,3}, L.J.Tacconi¹, D.Lutz¹, A. Saintonge⁴, S.Berta¹, B.Magnelli⁵, F.Combes⁶, S.García-Burillo⁷, R.Neri⁸, A.Bolatto⁹, T.Contini¹⁰, S.Lilly¹¹, J.Boissier⁸, F.Boone¹⁰, N.Bouché¹⁰, F.Bournaud¹², A.Burkert^{13,1}, M.Carollo¹¹, L.Colina¹⁴, M.C.Cooper¹⁵, P.Cox¹⁶, C.Feruglio⁸, N.M. Förster Schreiber¹, J.Freundlich⁶, J.Gracia-Carpio¹, S.Juneau¹², K.Kovac¹¹, M.Lippa¹, T.Naab¹⁷, P.Salome⁶, A.Renzini¹⁸, A.Sternberg¹⁹, F.Walter²⁰, B.Weiner²¹, A.Weiss²² & S.Wuyts¹

¹ Max-Planck-Institut für extraterrestrische Physik (MPE), Giessenbachstr., 85748 Garching, FRG

(linda@mpe.mpg.de, genzel@mpe.mpg.de)

² Dept. of Physics, Le Conte Hall, University of California, 94720 Berkeley, USA

³ Dept. of Astronomy, Campbell Hall, University of California, Berkeley, CA 94720, USA

⁴ Department of Physics & Astronomy, University College London, Gower Place, London WC1E 6BT, UK

⁵ Argelander-Institut für Astronomie, Universität Bonn, Auf dem Hügel 71, 53121 Bonn, FRG

⁶ Observatoire de Paris, LERMA, CNRS, 61 Av. de l'Observatoire, F-75014 Paris, FR

⁷ Observatorio Astronómico Nacional-OAN, Observatorio de Madrid, Alfonso XII, 3, 28014 - Madrid, SP

⁸ IRAM, 300 Rue de la Piscine, 38406 St.Martin d'Herès, Grenoble, France

⁹ Dept. of Astronomy, University of Maryland, College Park, MD 20742-2421, USA

¹⁰ Institut d'Astrophysique et de Planétologie, Université de Toulouse, 9 Avenue du Colonel Roche

BP 44346 - 31028 Toulouse Cedex 4, FR

¹Based on observations with the Plateau de Bure millimetre interferometer, operated by the Institute for Radio Astronomy in the Millimetre Range (IRAM), which is funded by a partnership of INSU/CNRS (France), MPG (Germany) and IGN (Spain).

- ¹¹ *Institute of Astronomy, Department of Physics, Eidgenössische Technische Hochschule, ETH
Zürich, CH-8093, SW*
- ¹² *Service d'Astrophysique, DAPNIA, CEA/Saclay, F-91191 Gif-sur-Yvette Cedex, FR*
- ¹³ *Universitätssternwarte der Ludwig-Maximiliansuniversität, Scheinerstr. 1, D-81679 München, FRG*
- ¹⁴ *CSIC Instituto Estructura Materia, C/ Serrano 121, 28006 Madrid, SP*
- ¹⁵ *Dept. of Physics & Astronomy, Frederick Reines Hall, University of California, Irvine, CA 92697*
- ¹⁶ *ALMA Santiago Central Office, Alonso de Córdova 3107, Vitacura, Santiago, CH*
- ¹⁷ *Max-Planck Institut für Astrophysik, Karl Schwarzschildstrasse 1, D-85748 Garching, FRG*
- ¹⁸ *Osservatorio Astronomico di Padova, Vicolo dell'Osservatorio 5, Padova, I-35122, IT*
- ¹⁹ *School of Physics and Astronomy, Tel Aviv University, Tel Aviv 69978, Israel*
- ²⁰ *Max Planck Institut für Astronomie (MPIA), Königstuhl 17, 69117 Heidelberg, FRG*
- ²¹ *Steward Observatory, 933 N. Cherry Ave., University of Arizona, Tucson AZ 85721-0065, USA*
- ²² *Max Planck Institut für Radioastronomie (MPIfR), Auf dem Huegel 69, 53121 Bonn, FRG*

ABSTRACT

We combine molecular gas masses inferred from CO emission in 500 star forming galaxies (SFGs) between $z=0$ and 3, from the IRAM-COLDGASS, PHIBSS1/2 and other surveys, with gas masses derived from Herschel far-IR dust measurements in 512 galaxy stacks over the same stellar mass/redshift range. We constrain the scaling relations of molecular gas depletion time scale (t_{depl}) and gas fraction (M_{molgas}/M_*) with redshift, specific star formation rate ($sSFR$) and stellar mass (M_*) in SFGs. The CO- and dust-based scaling relations agree remarkably well. This suggests that the CO \rightarrow H₂ mass conversion factor varies little within ± 0.6 dex of the main sequence line, and less than a factor of 2 throughout this redshift range. We find that t_{depl} scales as $(1+z)^{-0.3} \times (sSFR)^{-0.5}$, with no M_* dependence. The resulting steep redshift dependence of $M_{molgas}/M_* \propto (1+z)^3$ mirrors that of the $sSFR$ and probably reflects the gas supply rate. The decreasing gas fractions at high M_* are driven by the flattening of the SFR - M_* relation. At constant M_* , a larger $sSFR$ is due to a combination of an increasing gas fraction and a decreasing depletion time scale. As a result galaxy integrated samples of the M_{molgas} - SFR rate relation exhibit a super-linear slope, which increases with the range of $sSFR$. With these new relations it is now possible to determine M_{molgas} with an accuracy of ± 0.1 dex in relative terms, and ± 0.2 dex including systematic uncertainties.

Key words: galaxies: evolution — galaxies: high-redshift — galaxies: kinematics and dynamics — infrared: galaxies

1. Introduction

Stars form from dusty, molecular interstellar gas (McKee & Ostriker 2007, Kennicutt & Evans 2012). In the Milky Way and nearby galaxies arguably all star formation occurs in massive ($10^4 \dots 10^{6.5} M_{\odot}$), dense ($n(\text{H}_2) \sim 10^2 \dots 10^5 \text{ cm}^{-3}$) and cold ($T_{\text{gas}} \sim 10\text{-}40 \text{ K}$), ‘giant molecular clouds’ (GMCs) that are near or in virial equilibrium (Solomon et al. 1987, Bolatto et al. 2008, McKee & Ostriker 2007, but see Dobbs, Burkert & Pringle 2011, Dobbs & Pringle 2013). The star formation rates on galactic scales or star formation surface densities on sub-galactic scales down to a few kpc are empirically most strongly correlated with molecular gas (or dust) masses, or surface densities, while there is little or no correlation between star formation and neutral atomic hydrogen (Kennicutt 1989, Kennicutt et al. 2007, Bigiel et al. 2008, 2011, Leroy et al. 2008, 2013, Schrubba et al. 2011). However, it is not clear whether high molecular content as such is causally required for the onset of star formation (Glover & Clark 2012). Rather the key ingredients may be the combination of high gas volume density and sufficient dust shielding ($A_V > 7$, $\Sigma_{\text{gas}} > 100 M_{\odot} \text{ pc}^{-2}$) to decouple the dense cores from the external radiation field and allow it to cool and initiate collapse; these conditions may then also be conducive to molecule formation (Glover & Clark 2012, Krumholz, Leroy & McKee 2011, Heiderman et al. 2010, Lada et al. 2012).

About 90% of the cosmic star formation between $z=0$ and 2.5 occurs in galaxies that lie near the so-called ‘star formation main sequence’ (Rodighiero et al. 2011, Sargent et al. 2012), which is a fairly tight (± 0.3 dex scatter), near-linear relationship between stellar mass and star formation rate (Schiminovich et al. 2007, Noeske et al. 2007, Elbaz et al. 2007, 2011, Daddi et al. 2007, Panella et al. 2009, Peng et al. 2010, Rodighiero et al.

2010, Karim et al. 2011, Salmi et al. 2012, Whitaker et al. 2012, Lilly et al. 2013). From the NEWFIRM medium band survey in the AEGIS and COSMOS fields Whitaker et al. (2012) have proposed an analytic fitting function of the center line of this sequence as a function of redshift ($z < 2.5$) and stellar mass (for $M_* \geq 10^{10} M_\odot$)

$$\log(sSFR(ms, z, M_*)) = -1.12 + 1.14z - 0.19z^2 - (0.3 + 0.13z) \times (\log M_* - 10.5) \quad (\text{Gyr}^{-1}) \quad (1),$$

where the specific star formation rate $sSFR$ (Gyr^{-1}) is the ratio of star formation rate SFR ($M_\odot \text{yr}^{-1}$) and stellar mass M_* (M_\odot).

‘Main-sequence’ SFGs are characterized by disk, exponential rest-UV/rest-optical light distributions ($n_{\text{Sersic}} \sim 1-2$, Wuyts et al. 2011b) and a strong majority is rotation dominated (e.g. Shapiro et al. 2008, Förster Schreiber et al. 2009, Newman et al. 2013, Wisnioski et al. 2014). The tightness and time independent shape of the main sequence suggests that star forming galaxies grow along the sequence in an equilibrium of gas accretion, star formation and gas outflows (the “gas regulator model”: Bouché et al. 2010, Davé et al. 2012, Lilly et al. 2013, Peng & Maiolino 2014). At $z > 1$ main-sequence SFGs double their mass on a typical time scale of ~ 500 Myrs but their growth appears to halt suddenly when they reach the Schechter mass, $M_* \sim 10^{10.8..11} M_\odot$ (Conroy & Wechsler 2009, Peng et al. 2010). For a better understanding of the origin and evolution of this equilibrium evolution of the main sequence population, the goal of current studies is to establish how (efficiently) the conversion from cool gas to stars proceeds on a global galactic scale, and how this efficiency and the galaxies’ gas reservoirs change as a function of cosmic epoch (redshift), stellar mass, star formation rate, galaxy size/internal structure, gas motions and environmental parameters (see discussions in Tacconi et al.

2010, 2013, Daddi et al. 2010a,b, Genzel et al. 2010, Bouché et al. 2010, Lilly et al. 2013, Davé et al. 2011, 1012, Lagos et al. 2011, Fu et al. 2012).

The parameterization of the star formation main sequence as a function of redshift and stellar mass varies among different studies (Schiminovich et al. 2007, Noeske et al. 2007, Elbaz et al. 2007, 2011, Daddi et al. 2007, Panella et al. 2009, Rodighiero et al. 2010, Peng et al. 2010, Karim et al. 2011, Salmi et al. 2012, Lilly et al. 2013). This can be understood by different sample selections, survey completeness, methodology applied to derive M_* and $SFRs$, among other factors. Perhaps most importantly, the inferred slope of the main-sequence as a function of M_* depends on whether the sample is mass selected (including quenched galaxies leading to a steep slope, $d(sSFR)/d(\log M_*) = -0.3..-0.5$), or UV/optical magnitude-color selected (selecting mainly star forming galaxies, shallow slope, $d(sSFR)/d(\log M_*) = -0.1..0$). The Whitaker et al. (2012) fits (see also Whitaker et al. 2014) provide a good representation of the *actual locus* of the near-main-sequence SFGs in our samples, as well as that of the parent 3D-HST sample above $\log(M_*/M_\odot) \sim 10..10.2$, but their selecting on the basis of stellar mass means that the sample includes also quenched galaxies. In contrast a main-sequence with $d(sSFR)/d(\log M_*) \sim 0$ would be the expected slope of actively star forming galaxies growing in the equilibrium gas regulator framework (Lilly et al. 2013). The fact that at high stellar masses the slope of the main-sequence seems to steepen would then mean that the most massive star forming galaxies are beginning to drop below this ideal line and quench. We discuss in section 4.2 the impact of different parameterizations of the main sequence relation on the scaling relations.

To determine and quantify these dependencies, it is convenient to determine first the gas depletion time scale, t_{dep} , as a function of the above mentioned parameters

$$\begin{aligned} t_{dep} &= M_{gas}/SFR \quad \text{or,} \\ t_{dep} &= \Sigma_{gas}/\Sigma_{SFR} \quad (2), \end{aligned}$$

where M_{gas} and Σ_{gas} are the gas mass and surface density, SFR and Σ_{SFR} the total rate and surface density of star formation (the ‘‘Kennicutt-Schmidt’’ relation between gas and star formation rate, Kennicutt 1998). The first equation is appropriate for galaxy integrated, and the second for spatially resolved data.

Given the discussion above, it is most appropriate to concentrate here on the molecular gas depletion time scale, where the total gas mass and surface density on the right side of the equations in (2) are replaced by the molecular hydrogen mass and surface density, including the standard correction for helium (~36% in mass), and for the photo-dissociated surface layers of the molecular clouds that are fully molecular in H_2 but ‘dark’ (i.e. dissociated) in CO (Wolfire, Hollenbach & McKee 2010, Bolatto, Wolfire & Leroy 2013).

The virtue of the empirical depletion time scale (without any reference to its physical interpretation) is that it is easily accessible to global measurements of the standard tracers of star formation and gas (i.e. stellar and infrared luminosity, CO 1-0, 2-1, 3-2 line luminosity, HI mass, dust mass) in a large number of galaxies (e.g. Young & Scoville 1991, Solomon & Sage 1988, Gao & Solomon 2004, Scoville 2013). In the recent IRAM COLDGASS survey Saintonge et al. (2011a,b, 2012) have observed the galaxy integrated CO 1-0 line flux in 365 mass selected ($M_* > 10^{10} M_\odot$) SDSS galaxies between

$z=0.025\dots 0.05$. This homogeneously calibrated, purely mass selected survey can be directly connected to the properties of the overall SDSS parent sample. Saintonge et al. (2011b, 2012) find an average depletion time of about 1.2 Gyr for galaxies near the star formation main sequence (Brinchmann et al. 2004, Schiminovich et al. 2007), but a decrease in the depletion time above, and an increase in the depletion time scale below the main sequence, toward the sequence of passive galaxies. In the IRAM HERACLES survey Bigiel et al. (2008, 2011), Leroy et al. (2008, 2013) and Schruba et al. (2011) studied the spatial distribution of CO 2-1 emission on subgalactic scales (resolution ~ 1 kpc) in 30 local disk and dwarf star forming galaxies near the main sequence. They find a relatively constant depletion time scale of about 2.2 Gyrs.²

Once the depletion time scale is determined, baryonic molecular gas mass fractions can then be computed in a straightforward manner from

$$\frac{M_{mol\ gas}}{M_*} = \frac{M_{mol\ gas}}{SFR} \times \frac{SFR}{M_*} = t_{dep} \times sSFR \quad ,$$

$$\text{and } f_{mol\ gas} = \frac{M_{mol\ gas}}{M_{mol\ gas} + M_*} \quad (3).$$

Until a few years ago, studies of the gas content in $z>0.5$ galaxies were restricted to luminous, gas and dust rich, outliers, such as starbursts and mergers, significantly above the main-sequence line at their respective redshifts (e.g. Greve et al. 2005, Tacconi et al.

² the factor 2 (0.3 dex) difference in the depletion times inferred from the COLDGASS and HERACLES surveys owes to the combination of different computation of star formation rates, SED modeling in the former, and from UV+mid-IR or H α +mid-IR in the latter ($\sim 30\%$ effect), and the weighting scheme of different data points, integration over the entire galaxy in the former, and averaging individual line of sights with CO detections in the latter, including treatment of diffuse H α /IR emission ($\sim 60\%$ effect). This difference is well understood but might be taken as an estimate of the underlying systematic uncertainties. The calibration and methodology of the high- z data discussed in this paper is close to that of the COLDGASS survey approach, although for most galaxies in the PHIBSS1&2 surveys star formation rates are cross-calibrated to the UV+mid/far-IR scale through a “ladder” approach (Wuyts et al. 2011a).

2006, 2008, Riechers 2013, Carilli & Walter 2013, Bothwell et al. 2013). With the availability of more sensitive receivers at the IRAM Plateau de Bure mm-interferometer (PdBI: Guilloteau et al. 1992, Cox 2011, Tacconi et al. 2010, 2013, Daddi et al. 2008, 2010a), the start of the science phase of ALMA, and the availability of dust observations from the Herschel PACS and SPIRE instruments, this situation has started to change dramatically and rapidly. Nevertheless it is, and will be for the foreseeable future, unrealistic to expect that one can carry out direct (molecular) gas mass estimates for galaxy sample sizes approaching or comparable to those in the panoramic UV, optical/near-IR and mid-IR/far-IR surveys ($10^{4\cdots7}$ galaxies in the standard “cosmological” fields).

In the present paper we instead use the presently available data on star forming galaxies near and above the main sequence from the current epoch ($z\sim 0$) to the peak of the cosmic star formation activity ($z\sim 1-3$) to determine how the molecular depletion times (and gas fractions) vary with redshift, star formation rate and stellar mass. With scaling relations in hand, it is then possible to predict the molecular gas properties of larger samples just on the basis of these basic input parameters. We take advantage of the availability of both CO-based and dust-based molecular gas mass determinations over the same range in parameters to compare these independent methods, and in particular, establish, reliable ‘zero points’.

Throughout, we adopt a Chabrier (2003) stellar initial mass function and a Λ CDM cosmology with $H_0 = 70 \text{ km s}^{-1}$ and $\Omega_m = 0.3$.

2. Observations

2.1 CO observations

To explore the cold molecular gas in SFGs covering the entire redshift range from $z=0$ to 4, the stellar mass range of $M_*=10^{9.8}$ to $10^{11.8} M_\odot$, and at a given redshift and stellar mass, star formation rates from about 10^{-1} to 10^2 times the main-sequence star formation rate, we collected 500 CO detections of star forming galaxies near, below and above the main sequence from a number of concurrent molecular surveys with CO 1-0, 2-1, 3-2 (and in two cases 4-3) rotational line emission (Table 1). We include:

1. 216 detections and 1 stack detection (much below the main-sequence) of CO 1-0 emission above and below the main sequence between $z=0.025-0.05$ from the final COLDGASS survey with the IRAM 30m telescope (Saintonge et al. 2011a,b, 2014 in prep.). We note that the star formation rates in that survey had then been updated from earlier UV-/optical SED fitting (Saintonge et al. 2011a) with mid-IR star formation rates from WISE, (Saintonge et al. in prep., Huang & Kauffmann 2014);
2. 90 CO 1-0 detections with the IRAM 30m of $z=0.002-0.09$ luminous and ultra-luminous IR-galaxies (LIRGs and ULIRGs) from the GOALS survey (Armus et al. 2009), from the work of Gao & Solomon (2004), Gracia-Carpio et al. (2008, 2009, and priv. comm.), and Garcia-Burillo et al. (2012);
3. 31 CO 1-0 or 3-2 detections of (above main-sequence) SFGs between $z=0.06$ and 0.5 with the CARMA millimeter array from the EGNOG survey (Bauermeister et al. 2013);

4. 14 CO 2-1 or 3-2 detections at $z=0.6-0.9$ and 18 CO 1-0 detections at $z=0.2-0.58$ (significantly above-main-sequence) ULIRGs with the IRAM 30m telescope from Combes et al. (2011,2013);
5. 11 CO 2-1 or 3-2 detections of near main-sequence SFGs between $z=0.5$ and 3.2 from Daddi et al. (2010a) and Magdis et al. (2012a), obtained with the IRAM PdBI;
6. 6 CO 2-1 detections of $z=1-1.2$ main-sequence SFGs selected from the Herschel-PEP survey (Lutz et al. 2011), obtained with the IRAM PdBI (Magnelli et al. 2012);
7. 52 detections of CO 3-2 emission in main-sequence SFGs in two redshift slices at $z=1-1.5$ (38) and $z=2-2.5$ (14) as part of the PHIBSS(1) survey with the IRAM PdBI (Tacconi et al. 2010, 2013);
8. 31 detections (and 2 upper limits) of CO 2-1 or 3-2 in main sequence SFGs between $z=0.5$ and 1, and 3 at $z\sim 2$, as part of the PHIBSS(2) survey with the IRAM PdBI (Tacconi, Combes et al. 2014, in preparation);
9. 19 CO 2-1, 3-2 or 4-3 detections of above main-sequence submillimeter galaxies (SMGs) between $z=1.2$ and 3.4 , obtained with the IRAM PdBI by Greve et al. (2005), Tacconi et al. (2006, 2008) and Bothwell et al. (2013);
10. 8 CO 3-2 detections of $z=1.4$ to 3.2 lensed main-sequence SFGs obtained with the IRAM PdBI (Saintonge et al. 2013).

The redshift- $sSFR$ coverage of this sample is shown in Figure 1, with the different symbols denoting the various surveys mentioned in our listing above. Owing to the

sensitivity limits the overall distribution in z - $sSFR$ space is biased to SFGs above the main sequence. However, the more recent extensive surveys at the IRAM telescopes at $z\sim 0.03$ (COLDGASS), $z\sim 0.7$ (PHIBBS2), $z\sim 1.2$ (PHIBSS 1+2) and $z=2.2$ (PHIBSS1) have begun to establish a decent coverage of massive SFGs above and below the main-sequence line. Most of these data are benchmark sub-samples of large UV/optical/infrared/radio imaging surveys with spectroscopic redshifts, and well established and relatively homogeneous stellar and star formation properties. The COLDGASS sample is drawn from SDSS. PHIBSS (1,2) and the data of Daddi et al. (2010a), Magdis et al. (2012a) and Magnelli et al. (2012) are selected from deep rest-frame UV-/optical imaging surveys in EGS (Davis et al. 2007, Newman et al. 2013, Cooper et al. 2012), GOODS N (Giavalisco et al. 2004, Berta et al. 2010) and COSMOS (Lilly et al. 2007, 2009), including the recent CANDELS J- and H-band HST imaging (Grogin et al. 2011, Koekemoer et al. 2011) and 3D-HST grism spectroscopy (Brammer et al. 2012, Skelton et al. 2014), as well as D3a (Kong et al. 2006) and the BX/BM samples of Steidel et al. (2004) and Adelberger et al. (2004).

We have binned the 500 SFGs of our CO sample into 6 redshift bins (Table 1). The number of SFGs in each of the five higher z bins is comparable (28-49). The highest four bins have a good coverage of the main-sequence population, while the lowest of these bins ($z=0.05-0.45$) contains mostly above main sequence star bursting systems. There are few galaxies significantly below the main sequence, for the obvious reason of detectability. The lowest redshift bin (mostly COLDGASS) naturally contains by far the largest number of galaxies (296 of the 500 galaxies). This imbalance needs to be taken into account carefully when considering the scaling relations.

2.1.1 Derivation of molecular gas masses

Observations of giant molecular clouds (GMCs) in the Milky Way and nearby galaxies have established that the integrated line flux of ^{12}CO millimeter rotational lines can be used to infer molecular gas masses, although the CO molecule only makes up a small fraction of the entire gas mass, and its lower rotational lines (1-0, 2-1, 3-2) are almost always very optically thick (Dickman, Snell & Schloerb 1986, Solomon et al. 1987, Bolatto et al. 2013). This is because the CO emission comes from moderately dense (volume average densities $\langle n(\text{H}_2) \rangle \sim 200 \text{ cm}^{-3}$, column densities $N(\text{H}_2) \sim 10^{22} \text{ cm}^{-2}$), self-gravitating GMCs of kinetic temperature 10-50 K. Dickman et al. (1986) and Solomon et al. (1987) have shown that in this ‘virial’ regime, or if the emission comes from an ensemble of similar mass, near-virialized clouds spread in velocity by galactic rotation, the integrated line CO line luminosity $L'_{\text{CO}} = \int_{\text{source line}} \int T_R dv dA$ (T_R is the Rayleigh-Jeans source brightness temperature as a function of Doppler velocity v) is proportional to the total gas mass in the cloud/galaxy. In this ‘cloud counting’ technique the total molecular gas mass (including a 36% mass correction for helium) then depends on the observed CO $J \rightarrow J-1$ line flux $F_{\text{CO},J}$, source luminosity distance D_L , redshift z and observed line wavelength $\lambda_{\text{obs},J} = \lambda_{\text{rest},J} (1+z)$ as (Solomon et al. 1997)

$$\begin{aligned}
 M_{\text{gas}} / M_{\odot} &= \alpha_{\text{CO},1} \times L'_{\text{CO},1} \\
 &= 1.75 \times 10^9 \left(\frac{\alpha_{\text{CO},1} \times R_{1J}}{\alpha_{\text{MW}}} \right) \times \left(\frac{F_{\text{CO},J}}{\text{Jy km/s}} \right) \times (1+z)^{-3} \times \left(\frac{\lambda_{\text{obs},J}}{\text{mm}} \right)^2 \times \left(\frac{D_L}{\text{Gpc}} \right)^2 \quad (4).
 \end{aligned}$$

In general, in the virial regime, the conversion factor α depends on the average cloud density $\langle n(H_2) \rangle$, on the equivalent Rayleigh-Jeans brightness temperature T_{RJ} of the CO transition $J \rightarrow J-1$, and on metallicity Z (see Genzel et al. 2012 and Bolatto et al. 2013 for more detailed discussions of the observational evidence),

$$\alpha_{COJ} = \zeta \left(\frac{(\langle n(H_2) \rangle)^{1/2}}{T_{RJ}} \right) \times \chi(Z) \quad (5).$$

In the Milky Way and nearby star forming galaxies with near solar metallicity, as well as in dense star forming clumps of lower mass, lower metallicity galaxies, the empirical CO 1-0 conversion factor α_{CO1} determined with dynamical, dust and γ -ray calibrations are broadly consistent with a single value of $\alpha_{CO1} = \alpha_{MW} = 4.36 \pm 0.9 M_{\odot}/(K \text{ km/s pc}^2)$, equivalent to $X_{CO} = N(H_2)/(T_{RJ=1} \Delta v) = 2 \times 10^{20} \text{ (cm}^{-2}/(K \text{ km/s))}$, Strong & Mattox 1996, Dame, Hartmann & Thaddeus 2001, Grenier, Casandijan & Terrier 2005, Bolatto et al. 2008, Leroy et al. 2011, Abdo et al. 2010, Ostriker, McKee & Leroy 2010, Bolatto et al. 2013).

For galaxies of gas phase metallicity less than solar, the conversion factor and metallicity are inversely correlated, as the result of an increasing fraction of the molecular hydrogen gas column that is photo-dissociated, and as a result ‘dark’ in CO (Leroy et al. 2011, Genzel et al. 2012, Bolatto et al. 2013). Motivated by the theoretical work of Wolfire et al. (2010) on the photo-dissociation of clouds with a range of hydrogen densities and UV radiation field intensities, but with a constant hydrogen column, Bolatto et al. (2013) have proposed the following fitting function for $\chi(Z)$,

$$\chi(Z) = 0.67 \times \exp(0.36 \times 10^{-(12+\log(O/H)-8.67)}) \quad (6),$$

where $12+\log(O/H)$ is the gas phase oxygen abundance in the galaxy on the Pettini & Pagel (2004) calibration scale, with the solar abundance of 8.67 (Asplund et al. 2004). Equation (6) assumes an average GMC hydrogen column density of $100 M_{\odot} \text{ pc}^{-2}$, or $9 \times 10^{21} \text{ cm}^{-2}$. Genzel et al. (2012) have combined the local (Leroy et al. 2011) and high- z empirical evidence for a second fitting function,

$$\chi(Z) = 10^{-1.27 \times (12+\log(O/H)-8.67)} \quad (7).$$

For the near-solar metallicities typical for most SFGs in our overall sample (96% of the 1012 SFGs are between $12+\log(O/H)=8.55$ and 8.75 on the PP04 scale), equations (6) and (7) yield values for $\chi(Z)$ within ± 0.12 dex of each other. We thus took the geometric mean of (6) and (7) in estimating the gas masses from CO in this paper. Note that this approach is not applicable for significantly sub-solar metallicity galaxies. Between $12+\log(O/H) = 7.9$ and 8.4 equation (7) implies a >0.22 dex correction than equation (6).

To convert the CO 2-1 and 3-2 luminosities in the near main-sequence galaxies (at all redshifts) to an equivalent CO 1-0 luminosity we apply a correction factor of $R_{IJ} = L'_{CO 1-0} / L'_{CO J-(J-1)} \sim 1.3$ and 2 to correct for the lower Rayleigh-Jeans brightness temperature of the $J - (J-1)$ transition relative to 1-0. This ‘‘excitation’’ correction entails a combination of the Planck correction (for a finite rotational temperature), as well as a correction for the sub-thermal population in the upper rotational levels. For above main sequence SMGs and ULIRGs ($sSFR/sSFR(ms,z,M_*) > 4$) we take $R_{IJ} = 1.2, 1.9$ and 2.4 for the 2-1, 3-2 and 4-3 transitions. These correction factors are empirically motivated by recent CO ladder observations in low- and high- z SFGs (Weiss et al. 2007, Dannerbauer et al. 2009, Ivison et al. 2011, Riechers et al. 2010, Combes et al. 2013, Bauermeister et al. 2013, Bothwell

et al. 2013, Aravena et al. 2014). While there are undoubtedly galaxy to galaxy variations in these correction factors, the scatter of these excitation variations is unlikely to be greater than ± 0.1 dex, as judged from the recent data sets.

Our starting point in this paper thus is to use for all 500 SFGs

$$\alpha_{0J} = \alpha_{MW} \times \chi(Z) \times R_{IJ} \quad (8)$$

to derive molecular gas masses from CO observations.

2.2 Dust observations

As part of the Herschel-PEP (Lutz et al. 2011) and Herschel-HERMES (Oliver et al. 2012) far-IR continuum surveys, Magnelli et al. (2014) have established 100 to 500 μ m far-IR SEDs from stacking PACS and SPIRE photometry in 8846, 4753 and 254 749 K- and I-selected SFGs in the GOODS-N, GOODS-S and COSMOS fields, respectively. For details of the methodology we refer to Magnelli et al. (2014). Briefly, star formation rates are calibrated onto the Wuyts et al. (2011a) ladder of UV-, mid-IR and far-IR based indicators. Since the far-IR detection rate drops with increasing redshift and decreasing SFR and M_* , it is necessary to average many individual data points to determine good far-IR SEDs as a function of z , SFR and M_* . For this purpose, Magnelli et al. (2014) interpolated the data onto a three dimensional grid of 512 samples in z , SFR and M_* and then stacked the photometry in each bin. Next Magnelli et al. determined for each resulting SED the dust temperature, by fitting to model SEDs from the library of Dale

and Helou (2002), for which dust temperatures were established from single optically thin, modified blackbody fits with emission index $\beta=1.5$.

From these stacks we computed dust masses using Draine & Li (2007) models. The models were built following the procedure widely adopted in the literature, as prescribed by these authors, and limiting the parameter space to the range suggested by Draine et al. (2007) for galaxies missing sub-mm data. These restricted parameters ranges are based on the analysis of local SINGS galaxies by Draine et al. (2007). We used the the Li & Draine (2001) values of dust opacities as a function of wavelength. For more details we defer to Draine & Li (2007). As recognized by several authors, the Draine & Li (2007)-based dust masses turn out to be larger than those derived using single-temperature modified black body models. For example Magnelli et al. (2012) and Magdis et al. (2012) report a ratio of ~ 3 between the two estimates. It is not trivial to directly compare our results to these studies, because the assumptions and procedures followed are slightly different. First of all, it is worth to note that while Magnelli et al. (2012) adopt $\beta=1.5$ to associate a modified black body model to the Dale & Helou (2002) templates, the latter are defined with a variable β , depending on the intensity of the radiation field. Moreover, the Li & Draine (2001) dust opacities adopt $\beta=2.08$ (Li & Draine 2001, Draine & Li 2003). Bianchi (2013) and Berta et al. (in prep.) show that differences in β induce different ratios of the Draine & Li (2007) to the modified black body modeling. In addition, simulations by Berta et al. (in prep.) highlight that if the far-IR SEDs are not well sampled, e.g. if the maximum rest-frame wavelength covered by the available photometry is $\leq 160\mu\text{m}$, the inferred dust mass can be affected by systematics, with details depending on the values of the Draine & Li (2007) parameters. Only a small

fraction ($\sim 10\%$) of bins in the M_* - $sSFR$ - z grid are affected by these effects, however.

Keeping in mind these caveats, the Draine & Li (2007) model dust masses are on average 4.8 times larger than the estimate based on the modified black body modeling by Magnelli et al. (2014). On the other hand, this factor reduces to ≤ 1.5 if a direct modified black body fit with $\beta=2.08$ is carried out on the same stacked photometry. Our new estimation of dust masses yields

$$\left(\frac{M_{dust}}{M_{\odot}}\right) = 1.2 \times 10^{15} \left(\frac{SFR}{M_{\odot} yr^{-1}}\right) \times \left(\frac{T_{dust}(MBB)}{K}\right)^{-5.5} \quad (9).$$

The conversion to gas masses requires the application of a metallicity dependent dust to gas ratio correction, which also enters the redshift evolution through the redshift dependence of the mass-metallicity relation below (Bethermin et al. 2014). Following Magdis et al. (2012b) and Magnelli et al. (2012) we converted the Draine & Li (2007) model dust masses to (molecular) gas masses by applying the metallicity dependent dust to gas ratio fitting function for $z \sim 0$ SFGs found by Leroy et al. (2011)

$$\delta_{dg} = \frac{M_{dust}}{M_{molecules}} = 10^{(-2+0.85 \times (12+\log(O/H)-8.67))} \quad (10),$$

where $12 + \log(O/H)$ is the gas phase oxygen abundance (see also Draine et al 2007 for dust-to-gas with metallicity scalings of the SINGS nearby galaxy sample and Galametz et al 2011 for lower metallicity galaxies down to $12+\log(O/H)=8.0$). We note that the metallicity dependence in equation (10) is within a few percent of that found in the last section from averaging equations (6) and (7). This means that the metallicity (and hence, mass) corrections we choose in this paper for the dust and CO data are very similar.

As in the case of the CO sample, we binned the 512 stacks into 6 redshift bins comparable to those of the CO sample. These 512 stacks provide a complete and

unbiased estimates of the mean FIR/submm properties of all SFGs with $0 < z < 2$, $M_* > 10^{10} M_{\odot}$, and $\log(sSFR/sSFR(ms,z,M_*)) > -0.3$ (see Figs. 4 & 5 of Magnelli et al. 2014). In contrast to the CO sample, the dust sample has comparable numbers of SFGs (83-191) in the middle 4 redshift bins, while the number in the lowest and highest bins are significantly smaller (~ 30 each). This difference actually turns out to be advantageous in the discussion of the scaling relations below, as the dust sample is obviously not dominated in number by the lowest redshift bin.

2.3 Mass-metallicity relation

For the few SFGs in this paper with estimates of gas phase metallicities from strong line rest-frame optical line ratios, we determine individual estimates of $\log Z = 12 + \log(O/H)$. For instance, if the $\lambda 6583$ [NII] / $\lambda 6563$ H α line flux ratio is measured the Pettini & Pagel (2004) indicator yields

$$12 + \log(O/H)_{PP04} = 8.9 + 0.57 \times \log(F(6583 \text{ [NII]}) / F(6563 \text{ H}\alpha)) \quad (11).$$

However, for the majority of the SFGs in our CO and dust samples, such line ratios are not available and it is necessary, for the metallicity corrections discussed above, to refer to the mass-metallicity relation. The scatter in the above relation is ± 0.18 dex. Following Maiolino et al. (2008) we combined the mass-metallicity relations at different redshifts presented by Erb et al. (2006), Maiolino et al. (2008), Zahid et al. (2014) and Wuyts et al. (2014) in the following fitting function

$$12 + \log(O/H)_{PP04} = a - 0.087 \times (\log M_* - b)^2, \text{ with}$$

$$a = 8.74(0.06), \text{ and}$$

$$b = 10.4(0.05) + 4.46(0.3) \times \log(1+z) - 1.78(0.4) \times (\log(1+z))^2 \quad (12).$$

2.4 Stellar masses and star formation rates

For the COLDGASS sample the stellar masses and luminosities are calibrated in the frame of SDSS, GALEX and WISE (Saintonge et al. 2011a, 2012). For the various LIRG/ULIRG samples at $z \sim 0-1$ we refer to the original papers for a discussion of the stellar masses, which were converted, if necessary, to the Chabrier IMF adopted here. Infrared luminosities were obtained from the far-infrared (30-300 μ m) SEDs, assuming $L_{\text{IR}} = 1.3 \times L_{\text{FIR}}$ and star formation rates were estimated from Kennicutt (1998) with a correction to the Chabrier adopted here, $\text{SFR} (M_{\odot} \text{ yr}^{-1}) = 10^{-10} \times L_{\text{IR}} (L_{\odot})$ (see discussion in Genzel et al. 2010). In the case of $z < 1$ ULIRGs ($L_{\text{FIR}} > 10^{12} L_{\odot}$), we multiplied the observed luminosities by 0.75 to account for an average AGN contribution of 25%, as motivated by ISO observations (Genzel et al. 1998).

Global stellar properties for all optically/UV-selected high- z SFGs (both for the CO and dust-samples) were derived following similar procedures as outlined by Wuyts et al. (2011a). In brief, stellar masses were obtained from fitting the rest-UV to near-IR spectral energy distributions (SEDs) with Bruzual & Charlot (2003) population synthesis models, the Calzetti et al. (2000) reddening law, a solar metallicity, and a range of star formation histories (in particular including constant SFR, as well as exponentially declining or increasing SFRs with varying e-folding timescales). SFRs were obtained

from rest-UV+IR luminosities through the Herschel-Spitzer-calibrated ladder of SFR indicators of Wuyts et al. (2011a) or, if not available, from the UV-optical SED fits.

For submillimeter galaxies (SMGs) we adopted the stellar masses and luminosities of Magnelli et al. (2012, 2014, priv.comm.), the latter being derived from PACS/SPIRE Herschel SEDs and converted to star formation rates with the modified Kennicutt (1998) conversion as given above.

Note that throughout the paper we define stellar mass as the “observed” mass (“live” stars plus remnants), after mass loss from stars. This is about 0.15...0.2 dex smaller than the integral of the SFR over time.

3. Results

Several recent papers have attempted to quantify the dependence of galaxy integrated molecular gas depletion time scale (or its inverse, often called the “star formation efficiency”), and the related molecular gas fraction, on redshift, specific star formation rate and stellar mass. For instance, from COLDGASS and PHIBSS 1 CO data Tacconi et al. (2013) infer the logarithmic scaling index with redshift, $\zeta_{f1} = d(\log t_{depl})/d(\log(1+z))$, to range between -0.7 and -1, while Santini et al. (2014) find $\zeta_{f1} \sim -1.5$ from PEP Herschel dust data. Magdis et al. (2012b), Saintonge et al. (2012), Tacconi et al. (2013) and Huang & Kauffmann (2014) find that at a given redshift the depletion time scale decreases with increasing specific star formation rate relative to its value at the main-sequence line. The corresponding logarithmic scaling index, $\zeta_{g1} = d(\log t_{depl})/d(\log(sSFR))$, ranges between -0.3 and -0.45. However, the exact value of ζ_{g1} is strongly degenerate with variations of the CO conversion factor with $sSFR$ (Magdis et al. 2012b). The following analysis, for the first time based on a combination of CO and dust data sampled over a comparable range in redshift, specific star formation rate and stellar mass, promises to permit a major step forward in delineating these principal component dependences, and in particular, the role of the zero points (CO conversion factor, and dust model).

3.1 Separation of variables

In the left panel of Figure 2 we plot for the 6 redshift bins (different colored symbols) the CO-based depletion time scale as a function of normalized specific star formation rate offset from the main sequence line at a given redshift ($sSFR(ms, z, M_*)$, equation (1)). In this log-log presentation $\log(t_{depl})$ scales *linearly* with $\log(sSFR/sSFR(ms))$ over more

than 3 orders of magnitude in $sSFR$, from more than a factor of 10 below, to two orders of magnitude above the main-sequence, in the regime of the extreme outliers, such as $z \sim 0-0.5$ ULIRGs and some SMGs. This means that the dependence of t_{depl} on $sSFR$ is well fit by a single power law, to within the uncertainties dictated by the scatter of the relation. Fitting a power law to each of the $t_{depl} - (sSFR/sSFR(ms, z, M_*))$ z-sets shows no significant redshift evolution of the slope $\xi_{gI}(z) = d(\log t_{depl}(z)) / d \log (sSFR/sSFR(ms, z, M_*))$ (Figure 3). A weighted fit to the CO slope data in Figure 3 (filled blue circles) yields $d\xi_{gI}(z)/d \log(1+z) = -0.08 (\pm 0.13, 1\sigma)$. We note already here that there is also no evidence for a non-zero slope for the dust-based depletion time scales (black filled circles in Figure 3) discussed below (section 3.2), for which a weighted fit to the 6 redshift bins yields $d\xi_{gI}(z)/d \log(1+z) = +0.13 (\pm 0.18, 1\sigma)$.

A similar analysis in the $\log t_{depl} - \log M_*$ shows that a linear function (a power law in the original variables) with slope $0 (\pm 0.1)$ can account for the data in each of the redshift bins.

This is an important constraint. If a function of three independent variables (z , $sSFR$, M_*) is a power law in each of these variables, each with slope that does not depend on the other variable, then the function can be written as a **product of power law functions each dependent on one variable**. That means that the variables can be separated,

$$t_{depl}(z, sSFR, M_*)|_{\alpha=\alpha_0} = f_1(z)|_{sSFR=sSFR(ms, z, M_*)} \times g_1(sSFR / sSFR(ms, z, M_*)) \times h_1(M_*) \quad (13).$$

Here $f_1(z)$ tracks the dependence of t_{depl} on redshift at the main-sequence line (equation (1)), $g_1(sSFR/sSFR(ms, z, M_*))$ describes the dependence of t_{depl} on $sSFR$ relative to the

main-sequence line, and $h_I(M_*)$ delineates the stellar mass dependence. Now at first glance, the way we have written equation (13) (and analyzed the data) might seem a contradiction of the statement on variable separation above, since $g_I(sSFR/sSFR(ms,z,M_*))$ contains equation (1) in the denominator, which is a function of both z and M_* . However, equation (1) again is a product of power laws, so that the dependence of $sSFR(ms,z,M_*)$ can be easily pulled out of g_I . Equation (13) can then be resorted into a product of power laws of the individual variables ($z, sSFR, M_*$), as needed for separation. The slope of g_I remains unaffected by this renormalization. It turns out that because of the shallow mass dependence of equation, the mass dependence also does not change much when resorting g_I as a function of $sSFR$ only. The only function strongly affected is $f_I(z)$ since that now acquires a strong redshift dependence from equation (1.) This discussion already suggests that the separation of variables and the general conclusions on the quality of fits are independent of the choice of the main-sequence, which we will discuss in more detail in section 4.2. The depletion time scale may also depend on other parameters, such as bulge mass, gas volume and surface density, environmental density around the galaxy etc. but these dependencies cannot be explored with the current data sets.

If the parameter dependencies of t_{depl} can be separated according to equation (13), equation (3) shows that the parameter dependencies of molecular gas fractions can be separated as well,

$$\begin{aligned} \frac{M_{\text{molecular gas}}}{M_*}(z, sSFR, M_*)|_{\alpha=\alpha_{0,I}} &= t_{depl} \times sSFR \\ &= f_2(z)|_{sSFR=sSFR(ms,z)} \times g_2(sSFR / sSFR(ms, z, M_*)) \times h_2(M_*) \quad (14). \end{aligned}$$

We thus assume

$\log(g_1(sSFR / sSFR(ms, z, M_*)) = a_{g1} + \xi_{g1} \times \log(sSFR / sSFR(ms, z, M_*))$ (c.f. Saintonge et al. 2011b, 2012). In the first iteration we took the best fit constant slope from Figure 3 ($\xi_{g1}=-0.46$) and fitted the data in each redshift bin for the zero offset $a_{g1}(z)$. The resulting z-distribution of the zero offsets is shown in the right panel of Figure 2. Their z-dependence can again be well described by a power law, $\log(f_1(z)) = a_{f1} + \xi_{f1} \times \log(1+z)$.

In the second iteration we then removed the fitted zero-point offsets as a function of redshift by dividing the original data by $f_1(z)$ and fit the specific star formation rate dependences with a power law function, as above, but now for all 500 data points simultaneously. The result is shown in the right panel of Figure 2 and the left panel of Figure 4. We find that the best fitting parameters are $a_{f1}=-0.043 (\pm 0.01)$, $\xi_{f1}=-0.16 (\pm 0.04)$, $a_{g1}=0$, $\xi_{g1}=-0.46 (\pm 0.03)$. The numbers in the parentheses are the statistical 1σ fit uncertainties only; they do not include uncertainties due to systematics and cross-terms in the co-variance matrix.

The redshift dependence is shallower than found by Tacconi et al. (2013, $\xi_{f1}=-0.7\dots-1$). This is entirely due to the fact that we now quote the redshift dependence of the depletion time *on* the main-sequence line. Tacconi et al. (2013) instead took an average of the COLDGASS data ($\langle t_{depl} \rangle_{\text{COLDGASS}} (z=0)=1.5$ Gyr) and the $z=1.2$ PHIBSS data ($\langle t_{depl} \rangle_{\text{PHIBSS}} (z=1.2) =0.6-0.7$ Gyr), such that the logarithmic slope is -1. The COLDGASS sample has many massive galaxies below, while PHIBSS1 has mostly galaxies above the main sequence line, such that the average depletion times are biased high (at $z=0$) and low (at $z=1.2$) because of the negative slope in the left inset of Figure 2, resulting in an overestimate of the redshift dependence. The slope in the $\log t_{depl} - \log$

$sSFR/sSFR(ms,z,M_*)$ plane inferred above is in agreement with Saintonge et al. (2011b) and Huang & Kauffmann (2014) from COLDGASS data alone. One might also be concerned that the correlation between $\log sSFR$ and $\log t_{depl}$ might be biased due to the fact that the specific star formation rate is proportional to, and the depletion time is inversely proportional to star formation rate. This is correct in principle, of course, but simulations show that the impact of this intrinsic parameter correlation on our results is negligible because of the large dynamic range probed by the correlation in Figure 2 (2.5..3.5 dex), relative to the uncertainty in star formation rates ($\sim\pm 0.17$ dex).

The dispersion of the data in the left panel of Figure 4 around the best fitting power law function is ± 0.24 dex. This is quite tight given the *systematic uncertainties* in determining stellar masses and luminosities (± 0.15 dex), star formation rates (± 0.17 dex) and molecular gas masses ($>\pm 0.2$ dex), and the possibility of substantial variations of the CO conversion factor across the more than 3 orders of magnitude $sSFR/sSFR(ms,z,M_*)$ variation spanned by the data in Figure 4. There is perhaps a tendency for the $\log(t_{depl}/f_1)$ residuals as a function of $\log(sSFR/sSFR(ms,z,M_*))$ to exhibit an excess of negative values for $\log(sSFR/sSFR(ms,z,M_*)) > 0.6$. This may indicate that the depletion time scale above the main sequence, in the starburst-outlier regime, drops faster than captured by the power law fit above.

The right panel of Figure 4 explores whether the residuals $\log(t_{depl}/(f_1 \times g_1))$ depend on the remaining major internal parameter, the stellar mass. There appears to be no significant trend, in excellent agreement with the findings of Huang & Kauffmann (2014) at $z \sim 0$.

3.2 Dust based determination of t_{depl}

Next we repeat the same exercise for the dust based depletion time estimates from Herschel. The left panel of Figure 5 again shows the depletion time measurements as a function of $sSFR/sSFR(ms,z,M_*)$ in the 6 redshift bins. As for CO, the dust based depletion time scales do not exhibit a significant redshift evolution of $\check{\zeta}_{gI}(z) = d(\log t_{depl}(z) / d\log (sSFR/sSFR(ms,z,M_*)))$ (black filled circles in Figure 2), so that a constant slope $\check{\zeta}_{gI}=-0.59$ is an adequate description of the current dust data. The dependences of t_{depl} on redshift, specific star formation rate and stellar mass can again be written as a product of power laws, as in equations (13) and (14). Proceeding as before, we determine the zero-points of these power law functions in each bin, and plot these zero points as a function of redshift in the right panel of Figure 5 (black filled circles), along with the zero points of the CO-based determinations from Figure 2 (blue filled circles).

These totally independent estimates are *remarkably close*, especially given the possibly hidden systematic uncertainties, in CO conversion factor on the one hand, and in dust modeling and conversion from dust to gas on the other. There is a difference in slope ($\check{\zeta}_{fI}=-0.77 (\pm 0.19)$ for the dust-data compared to $\check{\zeta}_{fI}=-0.16 (\pm 0.04)$ for CO, as well as for their zero points ($a_{fI}=0.34 (\pm 0.08)$ for dust, compared to $a_{fI}=-0.04 (\pm 0.01)$ for CO) between the two data sets. However, on average the CO- and dust-based depletion time estimates as a function of redshift do not differ by more than $\sim 30\%$ between $z=0$ and 2.5. We note that an even better and more straightforward comparison would be the direct comparison of gas masses determined from each of the two techniques. This route is not possible, however, since the two samples do not significantly overlap, and in addition the

dust technique involves stacking a number of galaxies, rather than observing individual galaxies.

This remarkable similarity between CO- and dust-based scaling relations is further strengthened when comparing the $\log(t_{\text{depl}}/f_1) - \log(s\text{SFR}/\text{SFR}(m_s, z, M_*))$ and $\log(t_{\text{depl}}/(f_1 \times g_1)) - \log(M_*)$ distributions of CO (blue circles) and dust (red squares) in the left and right panels of Figure 6. The slope of the dust data in the specific-star formation rate scaling relation is somewhat steeper than that of the CO-data (dust: $\zeta_{g1} = -0.59 (\pm 0.05)$, CO: $\zeta_{g1} = -0.46 (\pm 0.03)$) but the overall distributions overlap over almost three orders of magnitude in $s\text{SFR}/\text{SFR}(m_s, z, M_*)$, from below the main sequence to extreme starburst outliers. The lack of a trend as a function of stellar mass also agrees in dust and gas (right panel of Figure 6). This excellent agreement of the separated scaling relations is also particularly relevant because of the very different redshift distributions of the CO- and dust-data in terms of numbers of SFGs per redshift bin. While the CO data in Figure 6 are heavily weighted toward the $z \sim 0$ COLDGASS measurements, the dust data are strongly weighted to $z \sim 1$. The agreement in scalings with $s\text{SFR}$ and M_* thus cannot be an artefact of biased redshift distributions.

Table 3 summarizes the fit parameters for the power law fitting functions for the CO- and dust-data. It also gives the parameters for an average between the gas and dust relations that might be considered the best current description of the molecular gas depletion time scaling relations.

3.2.1. *Global fits and error estimates*

For an alternative evaluation of the fits and their errors we went back and re-analyzed the CO- and dust-data in a different way. Instead of first binning in z -bins we carried out a direct global fit to data, assuming that the depletion times could be modelled as a linear function in the 3-space $\log(1+z)$, $\log(sSFR/sSFR(ms,z,M_*))$ and $\log M_*$. We then repeatedly fitted the 500 CO- and the 512 dust-data points, in each iteration perturbing the $sSFR/sSFR(ms,z,M_*)$ and t_{depl} values by ± 0.2 dex, as estimates of the full (statistical and systematic) errors. The fits results are in excellent agreement with the method discussed in section 3.1, indicating that the fit results are robust and the quoted errors are well captured by the error of the underlying parameters. We list these global fits values second in each of the entries of Table 3.

3.3 Scaling relations for M_{molgas}/M_*

Next we determined the equivalent relations for the molecular gas fractions. As discussed in the Introduction, once the scaling relations for t_{depl} are established, those for M_{molgas}/M_* in principle follow straightforwardly from equations (1) and (3). Given the slopes of the best fitting power laws in Table 3 one would then expect for the equivalent power law M_{molgas}/M_* -fitting function from equations (1),(3) and (14),

$$\begin{aligned}
\log(M_{\text{molgas}} / M_*(z, sSFR, M_*) |_{\alpha=\alpha_0}) &= \\
&= \log(f_2(z) |_{sSFR=sSFR(ms, z, M_*)}) + \log(g_2(sSFR / sSFR(ms, z, M_*))) + \log(h_2(M_*)) \\
&= a_{f_2} + \xi_{f_2} \times \log(1+z) + \xi_{g_2} \times \log(sSFR / sSFR(ms, z, M_*)) + \xi_{h_2} \times \log(M_*) \quad (15),
\end{aligned}$$

with slopes $\xi_{f_2} = \xi_{f_1} + 3.2 \sim +2.9$, $\xi_{g_2} = \xi_{g_1} + 1 \sim +0.5$, and $\xi_{h_2} = \xi_{h_1} - 0.3 \sim -0.3$.

In order to check for systematic effects, we decided to check the consistency of the scaling relations (together with equation (1)) for the CO and dust samples, by computing M_{molgas}/M_* for each galaxy (or galaxy stack) and then establish the scaling relations. Figures 7 to 10 show this fitting carried out for the CO data (Figures 7 & 8) and for the dust data (Figures 9 & 10).

Consistent with the results of the last section, the agreement between the CO- and dust-data again is very good. Again we fitted the data also with the global fit method described in section 3.2.1., establishing that both the best fit values and their uncertainties are robust and well captured by the most probable errors (statistical plus systematic) of the underlying parameters. The parameters of the best fitting power law functions are summarized in Table 4. We find $\xi_{f_2}=2.7$, $\xi_{g_2}=0.5$ and $\xi_{h_2}=-0.4$ for both the “binned” and the global fitting methods.

These slopes (and also the zero points) are within ~ 0.1 dex of the expectations from equation (3), and give a measure of the internal systematic uncertainties. We will come back to this topic in section 4.2.

3.4 Intermediate Summary

The depletion times and molecular gas to stellar mass ratios derived from two independent and very different techniques (CO and dust), with each ~500 measurements covering the redshift range from 0 to 2-3, the range in specific star formation rate from below to much above the main-sequence line at each redshift, and in stellar mass from 10^{10} to several $10^{11} M_{\odot}$ yield similar results, and to within the uncertainties the same scaling indices. We note here again that a more direct cross-check of the two techniques through a direct galaxy-by-galaxy comparison of their gas masses is not possible because of the lack of overlap of samples. The good agreement is by no means expected. On the contrary, most researchers in the field of ISM/star formation studies would probably have predicted offsets and trends between these techniques of 0.2-0.5 dex. We have only corrected the CO mass estimates for excitation and metallicity dependences, and the dust to gas mass ratios for metallicity dependence. Given the systematic parameter dependencies and uncertainties of the calibrations used in each of the two techniques the good agreement (in zero point and logarithmic scaling indices) thus is remarkable. On this basis, our analysis yields the following main results;

1. To first order, the dependences on redshift, specific star formation rate and stellar mass can be well separated into a product of three power law functions depending on the individual parameters;
2. The depletion time scale at the main sequence line changes only slowly with redshift ($t_{depl} \propto (1+z)^{-0.3 \pm 0.15}$, by a factor of 0.7 from $z=0$ to $z=2.5$), and is smaller than the Hubble time at all z . The molecular gas to stellar mass ratios and the specific star formation rates as a function of redshift track each other

fairly closely ($\propto (1+z)^3$). This finding in turn suggests that the factor of ~ 20 - 30 increase in galactic star formation rates between the local Universe and the peak of cosmic star formation rate at $z \sim 1-3$ is mainly driven by the increased supply rate of fresh gas, rather than changes in galaxy scale star formation efficiency (in starbursts with small t_{depl}). This is consistent with the “gas-regulator” model (Bouché et al. 2010, Tacconi et al. 2010, 2013, Daddi et al. 2010, Davé et al. 2012, Lilly et al. 2013);

3. Changes in specific star formation rate at constant z and M_* are due to a combination of variations in gas fraction and depletion time scale, in agreement with Saintonge et al. (2012) and Magdis et al. (2012b). Galaxies above the main sequence have larger gas fractions but also at the same time smaller depletion time scales (or equivalently, higher star formation efficiency), in approximately comparable measure, than galaxies at or below the main sequence. The dependence on gas fraction may reflect the time variation in the gas supply rate from the cosmic web. The increase in ‘star formation efficiency’ with $sSFR$ (by a factor of 20 from the lower envelope of the main-sequence to the star-bursting outliers above the main-sequence) may be driven by the internal properties of the star forming interstellar medium, such as the dense gas fraction (Lada et al. 2012, Juneau et al. 2009) in the more compressed, cuspier SFGs above the main sequence (Wuyts et al. 2011b, Elbaz et al. 2011). The increasing depletion times below the main sequence, especially at high masses, may also be a signature of suppression of

the gravitational instability by large shear velocities driving up the Q of the ISM (“morphological quenching”: Martig et al. 2009, Genzel et al. 2014).

4. In the Whitaker et al. (2012) prescription of the main-sequence as the actual locus of the star forming galaxy population (equation (1)), the molecular gas fractions decrease as a function of stellar mass ($M_{gas}/M_* \propto (M_*)^{-0.4}$) but the depletion time scale does not vary with stellar mass. If one would instead assume $d(sSFR)/d(\log M_*)|_{main\ sequence} = 0$, as in the ideal gas regulator model, the strong mass dependence of gas fractions is lessened or even disappears. That means that the dropping gas fractions of the actual SFGs at and above the Schechter mass ($\log(M_S/M_\odot) \sim 10.9$) are a direct consequence of the fact that these galaxies have specific star formation rates lower than SFGs on the ideal gas regulator line ($sSFR = \text{const}$). We interpret these findings as empirical evidence for the expected quenching process(es) that should happen near and above the Schechter mass.

4. Discussion

4.1 Parameter scalings of the CO-molecular gas mass conversion factor

Our results so far assume that the ratio of molecular gas mass to CO luminosity needs only a correction for metallicity and excitation (equation (8)); α_{CO} or X_{CO} is thus *assumed to not vary with z , $sSFR$ and M_** . In the following, we show quantitatively that this assumption is justified in the regime of self-gravitating molecular clouds, and how much variation is possible, from comparison of the dust- and CO-data. There have been several recent papers tackling the observational (Bolatto et al. 2013, Genzel et al. 2012, Magdis et al. 2012b, Magnelli et al. 2012) and theoretical (Narayanan et al. 2011, 2012, Feldmann et al. 2012 a,b) constraints of such α_{CO} -variations. All these studies predict a strong dependence of the conversion factor on metallicity, because of photodissociation (as discussed in the Introduction). This dependence is already captured in equations (6) & (7), and included in the assumptions on the conversion factor in equation (8). Figure 5 shows that the CO- and dust-zero points as a function of z on average agree to about 50% (0.18 dex), which in turn provides a constraint of possible redshift variations of α_{CO} . Taking the maximum difference between the CO- and dust-based depletion time scales in Figure 5 as an upper limit to a possible redshift variation of α_{CO} , this variation cannot be more than a factor 2 between $z \sim 0$ and 2.5.

The theoretical work predicts a significant dependence of α_{CO} on the specific star formation rate (Narayanan et al. 2011, 2012, Feldmann et al. 2012 a,b), and there is empirical evidence of 3-5 times smaller α_{CO} values in studies of $z \sim 0$ ULIRG outliers as compared to the Milky Way value (Scoville, Yun & Bryant 1997, Downes & Solomon 1998, c.f. Bolatto et al. 2013). Because of the inverse dependence of the conversion

factor on gas temperature (equation (5)), the conversion factor is expected to decrease with increasing $sSFR$ and increasing temperature, as long as the mean densities do not simultaneously increase to compensate for this dependence.

A sensitive and straightforward, quantitative test of the dependence of α_{CO} on $sSFR$ can be derived from the well determined dependence of dust temperature on $sSFR/sSFR(ms,z,M_*)$ in the Herschel dust data of Magnelli et al. (2014), assuming that in dense gas $T_{gas} \sim T_{dust}$. Such a test can, of course, also be made from the comparison of the dependence of depletion time estimates as a function of $sSFR/sSFR(ms,z,M_*)$ in Figure 6 (with the same result) but the test on the dust temperature distribution is more direct and does not depend on the dust modeling of Draine & Li (2007).

Following Magnelli et al. (2014) and Magdis et al. (2012b) the relation between molecular gas depletion time scale and dust temperature in the limit of optically thin far-IR dust emission (and optically thick dust absorption in the UV/optical) is given by

$$\frac{L_{IR}}{M_{dust}} = c_1 \times \frac{SFR}{M_{mol\ gas} \times \delta_{dg}(Z)} = c_1 \times \frac{1}{t_{depl} \times \delta_{dg}(Z)} = c_2 \times T_{dust}^{4+\beta} \quad (16),$$

where the metallicity dependent dust to molecular gas ratio δ_{dg} is given in equation (1)0, β is the logarithmic scaling index of the frequency dependence of dust emissivity ($\beta \sim 1.5$, Magnelli et al. 2014), and c_1, c_2 (as well as c_3, c_4, c_5 below) are constants. We now expand the CO-conversion factor (for J=1) as a function of the three main parameters to the linear terms in the log,

$$\begin{aligned} \log(\alpha_{CO\ 1}) &= \log(\alpha_{MW}) + \log(\alpha_{CO\ 10} / \alpha_{MW}) \\ &+ \varepsilon_z \times \log(1+z) + \varepsilon_Z \times (\log(Z) - \log(Z_\odot)) \\ &+ \varepsilon_{sSFR} \times \log(sSFR / sSFR(ms, z, M_*)) \\ &+ \varepsilon_* \times (\log M_* - 10.5) \end{aligned} \quad (17),$$

where ε_z , ε_Z , ε_{sSFR} , and ε_* are the logarithmic slopes of the variations of α_{CO} as a function of redshift, metallicity, specific star formation rate relative to that at the main sequence, and stellar mass offset from $\log M_* = 10.5$. We define α_{CO10} as the ‘zero point’ of the conversion factor, that is, its value at $z=0$, $sSFR = sSFR(ms, z, M_*)$, $\log M_* = 10.5$ and $Z = Z_\odot$. The metallicity dependence is assumed to follow equations (6) and (7) with $\varepsilon_Z \sim -1.2$. Next we can write

$$\begin{aligned} \log t_{depl} = \log \left(\frac{\alpha_{CO} \times L_{CO}}{SFR} \right) &= \log t_{depl} |_{\alpha_{CO} = \alpha_{MW}} + \log(\alpha_{CO10} / \alpha_{MW}) \\ &+ \varepsilon_z \times \log(1+z) + \varepsilon_Z \times (\log(Z) - \log(Z_\odot)) \\ &+ \varepsilon_{sSFR} \times \log(sSFR / sSFR(ms, z, M_*)) \\ &+ \varepsilon_* \times (\log M_* - 10.5) \quad (18), \end{aligned}$$

where the left side of the equation is the ‘true’ depletion time scale as given in equation (16), while the first term on the right side is the ‘observed’ depletion time scale under the assumption that $\alpha_{CO} = \alpha_{MW} = \text{const}$, as in Table 3 and equation (13),

$$\begin{aligned} \log t_{depl} |_{\alpha_{CO} = \alpha_0} &= a_{f1} + \xi_{f1} \times \log(1+z) + \xi_{g1} \times \log(sSFR / sSFR(ms, z, M_*)) + \\ &\xi_{h1} \times (\log(M_*) - 10.5) \quad (19). \end{aligned}$$

We show below that the dependence of the observed dust temperature on redshift, specific star formation rate offset and stellar mass can also be separated into the product of three power law functions (as for t_{depl} and M_{molgas}/M_*) to yield

$$\begin{aligned} \log T_{dust} &= a_{f3} + \xi_{f3} \times \log(1+z) + \xi_{g3} \times \log(sSFR / sSFR(ms, z, M_*)) + \\ &\xi_{h3} \times (\log(M_*) - 10.35) \quad (20). \end{aligned}$$

Equations (17), (18), (19) and (20) can then be combined to yield

$$\log(T_{dust}) = c_3 - \frac{1}{4 + \beta} \times \left[\begin{array}{l} (\xi_{dg} + \varepsilon_z) \times (\log Z - \log Z_\odot) + (\xi_{f1} + \varepsilon_z) \times \log(1 + z) + \\ (\xi_{g1} + \varepsilon_{sSFR}) \times \log(sSFR / sSFR(ms, z, M_*)) + \\ \xi_{h1} \times \log M_* \end{array} \right] \\ = c_4 + \xi_{f3} \times \log(1 + z) + \xi_{g3} \times \log(sSFR / sSFR(ms, z, M_*)) + \xi_{h3} \times \log M_* \quad (21),$$

which finally results in

$$0 = (0.35(\pm 0.14) - \log(\alpha_{CO\ 10} / \alpha_{MW})) + \\ (\xi_{dg} - \varepsilon_z) \times (\log Z - 8.67) + \\ (-\xi_{f1} - (4 + \beta) \times \xi_{f3} - \varepsilon_z) \times \log(1 + z) + \\ (-\xi_{g1} - (4 + \beta) \times \xi_{g3} - \varepsilon_{sSFR}) \times \log(sSFR / sSFR(ms, z, M_*)) + \\ (-\xi_{h1} - (4 + \beta) \times \xi_{h3} - \varepsilon_*) \times (\log M_* - 10.5) \quad (22).$$

This shows that the logarithmic slopes of the dependence of α_{CO} on Z , z , $sSFR/sSFR(ms, z, M_*)$ and M_* can be uniquely constrained from the scaling relations of t_{depl} and T_{dust} . If equation (22) is to be fulfilled everywhere in the sampled parameter space and the different variables on the right hand side are independent, each of the coefficients in front of the variables on the right hand side must be zero.

Figures 10 & 11 show the scaling relations of the dust temperature in the same 512 galaxy stacks as in Figures 5 & 6 and 9 & 10, and Table 5 summarizes the best fit values for the power law fitting function in equation (20).

With these fit parameters and the assumption that the Herschel dust observations provide ‘‘ground truth’’ we find

$$\begin{aligned} \alpha_{CO\ 10} &= 9.8 (\pm 3.2) \\ \varepsilon_z &= -0.9 (\pm 0.3) \\ \varepsilon_z &= -0.41 (\pm 0.15) \\ \varepsilon_{sSFR} &= 0 (\pm 0.03) \\ \varepsilon_* &= 0.066 (\pm 0.02) \end{aligned} \quad (23).$$

The inferred metallicity dependence of the CO-conversion factor is broadly consistent with equations (6) & (7) ($\epsilon_Z \sim -1.2 \pm 0.3$). The inferred redshift dependence implies that the conversion factor at $z \sim 2.2$ is ~ 0.7 times that at $z \sim 0$, which would of course then imply a steeper gradient $\xi_{\text{FI}} \sim -0.5$, as suggested by the dust depletion time (Figure 5). The fact that the inferred zero point of the conversion factor is twice α_{MW} is also consistent with the $z=0$ shift between dust- and CO-depletion times.

The most important and largely unexpected result is that the CO conversion factor depends little on $s\text{SFR}$, at least near the main-sequence. Across $\Delta \log(s\text{SFR}/s\text{SFR}(m_s, z, M_*)) = \pm 0.6$ the dust temperature measurements set an upper limit to a change in the CO conversion factor of 6% for the mean value, and of 25% if the 2σ uncertainties are included! This is indeed a remarkably strong constraint, which applies as long as the dust measurements provide a ‘ground-truth’ estimate, and if $T_{\text{dust}} \sim T_{\text{gas}}$. For more extreme outliers above the main sequence the dust temperature gradient in Figure 12 appears to steepen. At $\Delta \log(s\text{SFR}/s\text{SFR}(m_s, z, M_*)) \sim +1.2$ the residuals from the slope 0.086 power law fit (red-dotted line in Figure 12) is about 0.04 dex above the fit, which would imply a decrease of the conversion factor compared to the value from equation (8), to $\alpha_{\text{CO}} \sim 2.5$. Extrapolating to the still higher offsets in the regime of extreme $z \sim 0$ ULIRGs is consistent with $\alpha_{\text{CO}} \sim 1$, the value empirically estimated by Downes & Solomon (1998) and Scoville et al. (1997; see also Bolatto et al. 2013). Finally the last constraint on the stellar mass dependence implies a change of α_{CO} of less than 7% from 10^{10} to $10^{11} M_{\odot}$ in stellar mass.

4.2 Discussion of uncertainties

4.2.1. Final global fits

In order to create the best final estimates of the scaling relations, we finally averaged/combined the CO- and dust-based relation in the last rows of Tables 3 and 4, under the assumption that these data sets provide two independent estimates of “ground truth”. This “averaging” effectively means that we are using a solar metallicity 1-0 conversion factor of $\alpha_{\text{MW}} \times 10^{0.11} = 5.16$. We note that the Magnelli et al. (2012) calibration of the dust masses are 0.22 dex smaller than the DL07 fitting in this paper, such that the 0.36 dex difference of the zero points in Table 3 between dust and CO would be much reduced in this case. For the ‘parameter separated, binned’ method discussed in sections 3.1 and 3.2 we averaged the fit values of the scaling relation obtained with the two methods, respectively. For the ‘global’ fit column in Table 3 we first added 0.11 dex as a zero point correction to all CO-, and subtracted 0.11 dex from all dust-depletion time and M_{gas}/M_* values, to bring the CO and dust data on a common zero point, before then carrying out a global fit to all 1012 data points, as described in section 3.2.1. To within the systematic uncertainties of about ± 0.2 dex, ***the results of all the fitting parameters are robust to the changes in fitting technique and whether or not CO and dust data are used separately or combined.*** We recommend the global fits as our currently best estimates of the scaling relations (bold face numbers in Tables 3 & 4).

However, given these systematic uncertainties and the varying selection functions in the data used in our analysis, there are indeed differences at this level. This can be seen, for instance, by comparing the gas masses computed from the depletion time scaling relation in Table 3 to those computed from the gas to stellar mass ratio scaling relations

in Table 4. On average the latter are about 25% (0.1 dex) larger than the former, and larger source to source variations are possible in different parts of the parameter space, owing to cross terms in the relations of Table 3 & 4 and equation (1). Likewise the redshift dependence of the gas mass to stellar mass ratio ($\zeta_{f2}=2.77$, Table 4) is less by 0.12 (± 0.16) dex than what one would have expected from the redshift dependence of the depletion time scale ($\zeta_{f1}=-0.31$ (± 0.16)), the redshift dependence of the specific star formation rate in Whitaker et al. (2012, equation (1)), $d(sSFR(ms,z,M_*))/d(\log(1+z)) \sim 3.2$ and equation (3). Because of the lack of correlation of the depletion time scale with stellar mass, and its shallow dependence on redshift, we recommend using the fitting equations in Table 3 for calculating gas masses.

4.2.2. Dependence of the results on the prescription of the main-sequence

A significant source of uncertainty comes from the choice of the fitting function for the main-sequence $sSFR$ as a function of z and M_* (equation (1)), which we have assumed as ground truth. As we have stated in the Introduction the Whitaker et al. (2012) fitting function used throughout this paper does traces the location of the observed SFGs in this paper, as well as its parent samples between $z=0$ and 2.5 and at $\log M_* > 10.2$, quite well. However, it over-predicts SFR and $sSFR$ at lower stellar masses (which are not sampled in this paper), where a more accurate prescription has been proposed by Whitaker et al. (2014). There are significant variations in the main-sequence prescriptions proposed in the literature, depending on galaxy selection criteria, star formation and mass tracers used etc. (Schiminovich et al. 2007, Noeske et al. 2007, Elbaz et al. 2007, 2011, Daddi et al. 2007, Panella et al. 2009, Rodighiero et al. 2010, Peng et al. 2010, Karim et al. 2011,

Salmi et al. 2012, Lilly et al. 2013). These variations introduce differences in the specific star formation rate of the main sequence line, as well as in particular in the stellar mass dependence of the main sequence at a given redshift.

We have explored what happens if instead of the Whitaker et al. (2012) fitting function, the simpler function proposed in equation (2) of Lilly et al. (2013) is chosen. That function is a shallow single power law as a function of stellar mass ($sSFR(ms,z,M_*) \sim M_*^{-0.1}$), without a redshift dependence (or curvature) as in the Whitaker et al. (2012, 2014) prescriptions. As a result it does somewhat better below $10^{10} M_\odot$ but above $\log(M_*/4 \times 10^{10} M_\odot)$ the Lilly et al. (2013) function predicts too high star formation rates and overshoots the observed locus of SFGs. In terms of the specific star formation rate of the main sequence line at a given stellar mass and redshift and the stellar mass dependence, the Whitaker and Lilly fitting functions bracket the other prescriptions proposed in the literature. We repeated the global fitting with the Lilly et al. (2013) prescription and list the resulting fit parameters for the scaling laws in depletion time scale and gas to stellar mass ratio in the second to last columns of Tables 3 and 4. With the exception of modest changes in the overall zero points and in the logarithmic slopes as a function of stellar mass (expected because of the relative locations of SFGs and fit at high mass discussed in the last sentences), the differences to the fits with the Whitaker prescriptions are negligible. This is especially relevant for the dependence on the parameter $sSFR/sSFR(ms,z,M_*)$. This relative insensitivity to the ms-prescription is because the values of $sSFR(z,M_*)$ in Whitaker et al. (2012, 2014) and Lilly et al. (2013) agree quite well between $M_*=2$ to $10 \times 10^{10} M_\odot$, where most of our SFGs reside. The differences increase outside this mass range, where we have few galaxies ($< 2 \times 10^{10} M_\odot$),

or where these differences then lead to a slightly different slope in the $\log M_*$ scaling relation (ζ_{hl} parameter in the last column of Tables 3 & 4).

4.2.3. Fitting in $sSFR$ -space

Instead of using a main-sequence prescription, it is also possible to express g_1 and g_2 as function of $sSFR$ directly. These global fit results are listed in the last columns of Table 3 & 4. Since no main-sequence prescription is involved in this case $\xi_{f2} = \xi_{f1} \sim +1.2$, $\xi_{g2} = +0.5 = \xi_{g1} + 1$, and $\zeta_{h2} = \zeta_{h1} \sim -0.2$, as expected. The global fits in the second to last ($g_{1,2}(sSFR/sSFR(ms,z,M_*))$) and the last columns in Tables 3 and 4 ($g_{1,2}(sSFR)$) have the same formal scatter of ± 0.24 dex, consistent with the expected systematic uncertainties. As such the fits are equivalent. The main difference is in the interpretation of the resulting depletion time scales as a function of redshift, at constant specific star formation rate and stellar mass. In the $sSFR$ -description the depletion time scale appears to be a strong function of redshift ($\xi_{f1} \sim +1.2$). At constant $sSFR$ galaxy at $z=2$ has a 3.8 time greater depletion time scale as at $z=0$. This is not a physical effect, however, since specific star formation rates vary strongly with redshift. For instance a $SFR=100 M_\odot \text{ yr}^{-1}$ “ULIRG” SFG at $z=0$ is an extreme outlier starburst above the main sequence, with a correspondingly short depletion time scale, while an SFG of the same SFR at $z=2$ is a common main sequence object near equilibrium.

4.2.4. Impact of metallicity descriptions

A different choice in the metallicity dependences of the CO conversion factor (equations (6) & (8)) and of the dust to gas ratio (equation (10)) will also have a

significant impact of the final parameter values. The metallicity corrections in equations (6), (7) and (10) are calibrated at $z=0$ and are very uncertain below about 0.3 solar metallicity, which affects stellar masses below about $10^{10} M_{\odot}$, especially at $z>1$. The Leroy et al. (2011) calibration of the dust to gas ratios is strictly applicable only to $z=0$ and refers to the total (molecular plus atomic) gas column; its redshift evolution is not known. However, with the exception of a few SFGs at $z>2$ the stellar mass range of our sample implies a modest metallicity range (~ 0.2 dex for 97% of our SFGs) from slightly below to slightly above solar, resulting in a range of CO conversion factors of less than a factor 2. The same is true for the dust-to-gas ratios. Because of this fairly limited metallicity (or mass) range sampled in the galaxies considered here, a different metallicity scaling might change the zero point but the impact on scaling relations should be second order.

4.2.4 Systematic uncertainties and missing parameters

It is important to keep in mind that both CO- and dust- methods rely on several uncertain assumptions (cloud counting, near-virialized clouds, dust emissivity modelling) and have substantial systematic uncertainties (dust model and metallicity dependent corrections calibrated at $z\sim 0$, mass-metallicity relation). The dust data as well as the CO 2-1 and 3-2 data used for most of the high- z galaxies are only sensitive to $T\sim 20-40$ K dust/gas in star forming regions, and not to a component of cold gas and dust, or to dust/gas associated with the atomic interstellar medium. The latter results in an important correction at $z\sim 0$ (Saintonge et al. 2011a,b) but may not play a dominant role at high- z (Lagos et al. 2012). The proper way to interpret the scaling relations discussed in this

paper is that they refer to *the star forming gas*, and not to ‘sterile’ gas components in the outer parts of the galaxies, or in the galaxy disks but not participating in gravitational collapse.

Judging from the existing CO-ladder observations at both low and high z , the excitation corrections we have applied should be on average valid to ± 0.1 dex, at least for SFGs near the main sequence and for $J \leq 3$. The corrections are more uncertain for compact extreme starbursts (with highly excited ISMs), or for extended low temperature disk galaxies (with a significant component of < 20 K gas that would be missed in the CO 3-2 transition).

If the errors of the input parameters are estimated correctly (± 0.2 dex for each $sSFR/sSFR(ms, z, M^*)$ and t_{depl}), all these considerations suggest that the ‘average’ relations in Tables 3 and 4 should give the scalings of the depletion time scale and molecular gas to stellar mass ratio between $z=0$ to 2.5, $\log(sSFR/sSFR(ms, z, M^*))$ between -1 and +1, and $\log(M_*/M_\odot)$ from 10 to 11.5 to about ± 0.1 dex in relative terms, and ± 0.2 dex including systematic uncertainties.

4.3 Interpretation of the shallow redshift dependence of the depletion time

The slow change of the molecular gas depletion time with cosmic epoch ($t_{depl} \propto (1+z)^{0.31 \pm 0.15}$) is somewhat of a surprise. Considering again the definition of the depletion time in the context of the KS-relation (equation (2)), t_{depl} might naturally be thought to be proportional to the galaxy’s dynamical time, with the proportionality being the inverse of

the galaxy's star formation efficiency ε (Silk 1997, Elmegreen 1997, Kennicutt 1998, Genzel et al. 2010). In the Mo, Mao & White (1998) framework of disk formation in a dark matter dominated Universe, the disk's dynamical time $t_{dyn}(R_d)$ (expressed in terms of its scale length R_d and maximum rotation velocity v_d) is tied to the properties of the dark matter halo, such that

$$t_{depl} = \frac{t_{dyn}(R_d)}{\varepsilon} = \frac{1}{\varepsilon} \times \frac{R_d}{v_d} = \frac{\lambda R_h}{\varepsilon \times C_h v_h} = \frac{\lambda}{\varepsilon C_h} \times 0.1 H(z)^{-1} \quad (24).$$

Here R_h and v_h are the halo size and circular velocity, and C_h is the ratio of the disk's rotation velocity to the halo circular velocity, which depends on the halo concentration (Bullock et al. 2001a). The parameter λ is the angular momentum parameter of the baryons ($\langle \lambda \rangle_{\text{dark matter}} \sim 0.04$, Bullock et al. 2001b), and $H(z) = H_0 \times (\Omega_A + \Omega_0 \times (1+z)^3)^{1/2}$ is the Hubble parameter. In a matter dominated Universe (applicable at high- z) the depletion time should then be proportional to $(1+z)^{-3/2}$ (see Davé et al. 2011), which is inconsistent with our results. A more careful evaluation requires two corrections. First the Hubble parameter in a Λ CDM Universe changes more slowly at late times. If one approximates $H(z) \propto (1+z)^\beta$, the average β for the redshift range $z=0$ to 2.5 is -0.98. Second the concentration parameter of dark matter halos was smaller at high- z than at $z=0$ (Bullock et al. 2001a), such that $C_h \sim 1.025$ at $z \sim 2.5$ and 1.24 at $z \sim 0$ (see Somerville et al. 2008). Taken together these two effects change the effective redshift dependence in equation (16) to $(1+z)^\beta$ with $\beta = -0.83$ (again between $z=0$ and 2.5). In a recent evaluation of star forming disk sizes in CANDELS/3D HST between $z=0$ and 3 van der Wel et al. (2014) find empirically $\beta = -0.75 (\pm 0.05)$, which is smaller than $\beta = -0.83$ but comes close to it. Additional baryonic processes connected to the processing/dissipation of the angular

momentum from the scale of the cosmic web to the inner, star forming disk and feedback processes inside the disk can both increase and decrease λ of the baryonic component (Dutton et al. 2011, Danovich et al. 2014). Empirically the average observed λ of the star forming gas at $z \sim 0.8-2.5$ is about 0.035, which is (fortuitously) close to the dark matter λ (Burkert et al. in preparation).

It is not yet clear whether the difference between the values of van der Weel's -0.75 (± 0.05) and estimates -0.31 (± 0.15) of the slope in the redshift dependence of the depletion time is highly significant. If it were, the shallow slope would indicate that the depletion time scale is not set by the global galactic dynamical time but by local processes. There are good reasons for this view. Cloud collapse and star formation are local processes that proceed on the free fall time τ_{ff} , which depends on the inverse square root of the local gas density (e.g. Krumholz & McKee 2005, Krumholz, Dekel & McKee 2012). Empirically Leroy et al. (2013) find from spatially resolved observations of the KS-relation in 30 $z \sim 0$ disk galaxies that the depletion time is near constant and independent of the local or global orbital times. However, the high- z disk galaxies in our sample appear to be globally marginally stable systems with a Toomre parameter $Q \lesssim Q_{crit} \sim 1$. In this case it is easy to show that the depletion time scale in the KS-relation on large scales is tied to the average galactic orbital time, even if in principal the local volumetric star formation rate density is tied to the local free fall time scale (e.g. Genzel et al. 2010, Krumholz, Dekel & McKee 2012). The dependence of depletion time scale on specific star formation rate ($t_{depl} \propto (sSFR/sSFR(ms, z, M_*))^{-1/2}$) will be discussed below (point 4) and can be considered another argument in favour of a local origin of the depletion time scale.

4.4 Impact on the gas – star formation relation

The scaling relations in Tables 3 & 4 can be used to predict the form of the galaxy integrated molecular gas – star formation relations at different redshifts and under varying selection functions. Because of the strong dependence of the depletion time on specific star formation rate ($t_{depl} \propto sSFR^{-0.5}$) the relation between $M_{mol\ gas}$ and SFR (the “molecular” KS-relation, Kennicutt 1998) becomes super-linear for a sample of SFGs with a spread in $sSFR$, although intrinsically the relation at constant $sSFR$ is linear.

We explored the impact of this dependence more quantitatively, by creating mock galaxy samples at different redshifts and varying spread in $sSFR/sSFR(ms, z, M_*)$ and establishing the resulting $M_{mol\ gas}$ - SFR from the relations in equation (1) and Table 3. For this purpose we repeatedly drew samples of 10-100 SFGs at a given z (the upper value is an upper limit to the samples available now and in the near future, at least for $z > 0.5$). At each redshift we varied redshifts by ± 10 -30% around the mean redshift and varied stellar masses from $\log(M_*/M_\odot) = 10.3$ to 11.3. We also varied SFR and $M_{mol\ gas}$ estimates by $\pm 0.1 \dots \pm 0.15$ dex to reflect measurement uncertainties, as well as $\Delta(\log(sSFR/sSFR(ms, z, M_*)))$ to sample the vertical direction in the M_* - SFR plane.

At all z , the resulting integrated KS-slope $N = d\log(SFR)/d(M_{mol\ gas})$ in this mock data sets approaches ~ 1 for large N and a small range in $sSFR$. However, even for a pure main-sequence sample $\Delta(\log(sSFR/sSFR(ms, z, M_*))) = \pm 0.3$ the slope becomes super linear, $N \sim 1.1$ -1.2, and with a substantial scatter of ± 0.07 dex resulting from the variation in SFG parameters. The scatter naturally increases with the decreasing number n_G of galaxies in the sample, from ± 0.06 for $n_G = 50$ -100, to ± 0.13 for $n_G = 20$, to ± 0.2 for $n_G = 10$. The slope

increases with the range of $sSFR$, from $N=1.08$ for $\Delta(\log(sSFR/sSFR(ms,z,M_*)))=\pm 0.3$, to $N=1.33$ for $\Delta(\log(sSFR/sSFR(ms,z,M_*)))=\pm 0.6$, and to $N=1.6$ for $\Delta(\log(sSFR/sSFR(ms,z,M_*)))=\pm 1$. Finally the slope for fixed $\Delta(\log(sSFR/sSFR(ms,z,M_*)))$ increases by about 0.2 from $z=0$ to $z=2$.

These findings are in excellent agreement with the integrated galaxy KS-slopes in the literature, both at low- z (Kennicutt 1998, Bigiel et al. 2008, Leroy et al. 2013, Saintonge et al. 2012), as well at $z \geq 1$ (Daddi et al. 2010b, Genzel et al. 2010, Tacconi et al. 2013). In particular the dependence of the slope on $\Delta(\log(sSFR/sSFR(ms,z,M_*)))$ is in excellent agreement with the findings of Kennicutt (1998), Daddi et al. (2010b), Genzel et al. (2010), Magdis et al. (2012) and Tacconi et al. (2013). Note that for galaxy samples with extreme selection functions, such as a combination of a near-main sequence sample with a sample of starburst outliers (such as studied by Daddi et al. 2010b and Genzel et al. 2010), the continuous change in t_{depl} with $sSFR$ would then to be appear like a dichotomy of two separate gas-SFR relations.

For lack of size information we cannot study here the more common KS-surface density relation $\Sigma_{mol\ gas}-\Sigma_{SFR}$. Whether or not extra factors come into play in the surface density relation as compared to the integrated quantities depends on the underlying physical reason of the $sSFR$ -dependence of t_{depl} and the probably connected inverse scaling of sizes with $sSFR$ (Wuyts et al. 2011b, Elbaz et al. 2011). Krumholz, Dekel & McKee (2012) have pointed out that if the KS-relation intrinsically is a volumetric relation between the gas and star formation volume densities, $\rho_{SFR} \propto \rho_{gas} / \tau_{ff}(\rho_{gas})$, the scale height h_{gas} of the gas comes in as an additional factor, such that the galaxy averaged surface density relation becomes

$$\Sigma_{SFR} = \langle \rho_{SFR} \times h_{gas} \rangle \propto h_{gas}^{-1/2} \times \langle \rho_{gas} \times h_{gas} \rangle^{3/2} \propto h_{gas}^{-1/2} \times \Sigma_{gas}^{3/2} \quad (25),$$

since the local free fall time scale $\tau_{ff}(\rho_{gas}) \propto \rho_{gas}^{-1/2}$. If the scaling $t_{depl} \propto sSFR^{-1/2}$ is physically connected with average local gas densities increasing with sSFR, as indicated by the findings of Wuyts et al. (2011b) and Elbaz et al. (2011), equation (24) would be in qualitative agreement with our scaling relation, with the addition of the scale height factor.

4.5 Dust or CO method?

We have shown that the derivation of molecular gas masses in star forming galaxies either from low-J CO rotational line emission (using a CO conversion ‘function’ that is solely dependent on metallicity, and contains a simple excitation correction), or from full far-infrared SEDs (with a conversion to gas mass that uses the Draine & Li (2007) dust model, a metallicity dependent gas to dust ratio function from Leroy et al. (2011), and the mass-metallicity relation), yield consistent results across a wide range of redshift, ratio of sSFR to that at the main-sequence of star formation, and stellar mass. To the extent that these two independent methods constrain the ‘ground truth’ the combined scaling relations in Tables 3 to 5 capture the most important variations of molecular gas depletion time scale, molecular to stellar mass ratios and dust temperature, within the ± 0.24 dex, ± 0.24 dex and ± 0.033 dex scatter of the three relations, and to an absolute level of $\pm 25\%$.

Extrapolating to future work in the measurement of cold gas masses in galaxies, it is likely that the focus will be on expansion of the statistics and parameter range on the one hand, including studies of the dependence on parameters that we have not been able to

explore (such as galaxy morphology and environment). On the other hand spatially resolved measurements are likely to play an increasingly important role, especially at higher redshift, in order to explore the dependence of depletion time scale (or its inverse, star formation ‘efficiency’) and gas fraction on internal galaxy structure, such as bulge to disk mass ratio, molecular volume and surface densities, clumpiness and internal galaxy kinematics, including galactic turbulence. The latter measurements will call for high resolution data benefitting naturally from or even requiring the availability of molecular kinematics that comes for free in line measurements of CO, HCN etc.

The former goal primarily requires *efficient* measurements of galaxy integrated gas masses. To this end, it is well known that the detection of a given gas mass from broad-band detection of its submillimeter dust emission is substantially faster than from CO 2-1 or 3-2 data. In the case of ALMA the detection of a molecular gas mass of $10^{10} M_{\odot}$ from band 7 (350 GHz) broad-band data requires only a few minutes at $z \sim 1-2$ (for a 5σ detection), while a CO-based measurement (again at 5σ) requires more than one hour at $z \sim 0.6-1$ and several hours at $z \sim 2$ (Scoville 2013, Scoville et al. 2014)³.

For these reasons, Scoville (2013) and Scoville et al. (2014) have proposed that a single frequency, broad-band measurement in the Rayleigh-Jeans tail of the dust SED (for instance at 345 GHz) is sufficient to establish dust and thus, gas masses. Scoville and his colleagues argue that the variation of dust temperature on galactic scales is sufficiently small, such that the assumption of a constant dust temperature, $T_0 \sim 25$ K, is justified. Qualitatively this assumption is indeed supported by the slow changes of T_{dust}

³ The integration times quoted here and shown in Figures 14 & 15 are for 34 active 12 m antennas, 7.5 GHz bandwidth in dual polarization for the dust measurements and do not include overheads. The integration times in Figures 14 & 15 are for the combination of the two bands. As per ALMA exposure calculator the assumed water vapor column for the highest frequency band 9 is less than 0.47mm, for band 7 is less than 0.66mm and for band 6 is less than 1.3mm.

with redshift and specific star formation rate in the Herschel data (Magnelli et al. 2014) we presented in Figures 11 & 12. Based on SCUBA observations of a subset of the sample of $z \sim 0$ disks from Draine et al. (2007), Scoville et al also argue that the dust to gas ratio does not vary significantly with metallicity ($\delta_{dg} \sim 0.0067 \sim \text{const}$). This assumption is obviously at tension with the Leroy et al. (2011) scaling relation in equation (10) that predicts a fairly strong metallicity dependence of δ_{dg} . This tension needs to be resolved in future studies.

The ‘Rayleigh-Jeans tail’ method thus is based on a single broad-band flux measurement, using calibrations of the 350 GHz dust emissivity to dust/gas mass from Planck observations in the Milky Way (Planck Collaboration 2011a,b) and of the nearby SINGS galaxies (Draine et al. 2007), yielding

$$\left(\frac{M_{\text{molgas}}}{1 \times 10^{10} M_{\odot}} \right) = \left(\frac{S_{350} D_L^2}{\text{mJy} \times \text{Gpc}^2} \right) \times (1+z)^{-(3+\beta)} \times \left(\frac{V_{\text{obs}}}{350 \text{ GHz}} \right)^{-(2+\beta)} \quad (26),$$

for $T_{\text{dust}} = 25 \text{ K}$, the above calibration of $\kappa_{\text{dust}}(350 \text{ GHz})$ (Scoville et al. 2014) and $\beta = 1.8$.

It is instructive to compare this method to more detailed measurements that would include the temperature variations in Table 5, the full Planck formula of the dust modified grey-body emission, and the Leroy et al. (2011) recipe for $\delta_{dg}(Z)$ (equation (10)).

For this purpose we built a simulation to verify the performance of equation (26) on simulated data points with the above assumptions. We use the scaling relations in Tables 4 and 5 to define a grid of modified Black Body SEDs (MBBs) in the M_* - $sSFR$ - z space, using the binning by Magnelli et al. (2014). Each point of the grid is characterized by M_* , $sSFR$, z , T_{dust} and M_{molgas} . We convolved the MBBs with a box filter centered on ALMA's band 7 (350 GHz), and computed the resulting flux density (in mJy). We then added

Gaussian noise as computed for a given integration time from the ALMA sensitivity calculator assuming 34 12-meter antennas, given as the default in the cycle 2 time estimator. This resulting ‘observed’ flux density is then converted to M_{molgas} using equation (26). Figure 13 (left panel) presents the result of the simulation and compares input to output gas masses. This Figure shows that the Rayleigh-Jeans approximation in equation (26), and assuming no metallicity dependent dust to gas ratio, leads to a ***significant underestimate of all inferred gas masses*** (on average -0.3 dex), and to artificial ***systematic trends throughout the probed parameter space*** (± 0.4 dex), and especially at high- z .

A first order improvement comes from introducing a constant Planck correction for all galaxies in any sample. For $T_{dust}=T_0= 25K=const$ one multiplies equation (26) with

$$\Gamma_{Pl} = \frac{\exp(h\nu_{obs}(1+z) / kT_0) - 1}{h\nu_{obs}(1+z) / kT_0} \quad (27),$$

where $\nu_{obs}=350$ GHz (Scoville et al. 2014). The central panel in Fig. 12 shows that with this global Planck correction the overall underestimate of gas masses is corrected and in fact over-compensated, mainly because the adopted value of T_0 is below the actual mean dust temperature near the main sequence. The large (± 0.35 dex) systematic trends remain because of the intrinsic variation in T_{dust} in Table 5 and the dust to gas ratio variations as a function of metallicity/mass. Correcting for the latter effect with the mass-metallicity relation in equation (10) improves the estimates further (right panel of Figure 13) but the temperature variations still cause significant systematic trends that should be accounted for in future studies attempting to measure fairly accurate relative trends in gas mass or depletion time. Obviously if the scaling relations in Table 5 are applicable to the galaxy sample a full Planck-correction with a variable T_{dust} can be executed with equation (27),

which should then give the correct output gas masses, making the single band technique indeed an efficient method for determining gas masses for large samples.

If one does not wish to rely on the scaling relations in Table 5, a dust temperature must be established for every individual galaxy. This can be done from measurements in two ALMA bands, exploiting the frequency dependence of the Planck correction in equation (27). We have simulated the performance of such a two-band technique, starting with 10σ photometry in either the band 6 (240 GHz) and band 7 (350 GHz) combination (Figure 14), or the band 7 and band 9 (670 GHz) combination (Figure 15). The band 6/7 combination has the advantage of less demanding observing conditions but delivers less accurate output dust temperatures (left panels in Figure 14) and gas masses (middle panels in Figure 14). For 10σ photometry the resulting precision of gas masses is not better than 0.7. The band 7/9 combination performs better in this respect (by about a factor of 2) but band 9 observations require much better, and thus somewhat rarer atmospheric conditions. For the quoted precisions, the total observing times for an input gas mass of $\sim 10^{10} M_{\odot}$ are >100 minutes at $z \sim 0.6-2.2$. At least for $z > 1.5$ this is still somewhat more favourable than CO detections (which are usually done in the 3mm atmospheric window) but the requirement of band 9 measurements for many galaxies likely will be quite restrictive in terms of sample size.

5. Conclusions

In this paper we have presented CO- and Herschel dust-based scaling relations of molecular gas mass depletion time, of the molecular gas mass to stellar mass ratio, and of the dust temperature as a function of redshift, specific star formation rate offset and stellar mass, for each ~ 500 star forming galaxies (or stacks of star forming galaxies) between $z \sim 0$ and 3. This is the first time that both dust and CO data have been compared in a large sample and on an equal footing across such a wide redshift range, and spanning 3 order of magnitude in specific star formation rate and 1.8 orders of magnitude in stellar mass.

Given the rather controversial discussion in the past decades on possible large variations in the CO to molecular gas mass conversion factors, and the expected very large uncertainties in gas mass estimates, our study reveals a remarkable convergence in the absolute zero points (absolute gas masses on the main sequence line as a function of redshift), and scalings with specific star formation rate offsets and stellar mass of the CO- and dust-based data once the metallicity dependence of the CO conversion factor and the gas to dust mass ratio are taken into account. Dust- and CO-based molecular gas masses agree to better than 50% throughout this large sampled range of parameters, and logarithmic scaling indices (power law exponents) agree to within fitting uncertainties of typically ± 0.1 . We show that this similarity sets stringent limits on changes of the CO conversion factor with redshift (less than a factor of 2 from $z=0$ to 2.5) and especially specific star formation rate (less than 25% across the main sequence). Our main findings are

- the metallicity dependence of gas to dust ratios and of the CO conversion factor track each other ($d \log sSFR / d \log (1+z) \sim d \log (M_{mol\ gas} / M_*) / d \log (1+z) \sim 3 (\pm 0.25)$);
- depletion time scales on the main–sequence line change only slowly with redshift ($d(\log t_{depl}) / d(\log(1+z)) = -0.3 (\pm 0.15)$), suggesting that the galactic scale star formation processes are similar across cosmic time. As a result the ratio of molecular gas to stellar mass ratio tracks the evolution of specific star formation rates, and both are plausibly controlled by the gas cycling into and out of galaxies;
- depletion times change significantly with the ratio of the sSFR to that at the star formation main sequence in specific star formation rate ($(d(\log t_{depl}) / d(\log(sSFR/sSFR(m_s, z, M_*))) = -0.5 \pm 0.01$) and do not change significantly with stellar mass. This in turn means that moving up in star formation rate at constant z and M_* means increasing gas fractions and simultaneously lower depletion time scales, in about equal measure. The increase in ‘star formation efficiency’ with sSFR may be driven by internal parameters, such as the dense gas fraction (Lada et al. 2012) for the more compressed, cuspier SFGs above the main sequence (Wuyts et al. 2011b, Elbaz et al. 2011);
- gas fractions drop with increasing stellar mass because the star formation sequence flattens at the highest stellar masses near and above the quenching mass (the Schechter mass), plausibly as a result of feedback.

- Because of the dependence of the depletion time scale on specific star formation rate (at a given redshift) observations of the galaxy integrated relation between molecular gas and star formation rate (the KS-relation) in a sample of star forming galaxies will exhibit a super-linear slope, although the intrinsic relation (at constant $sSFR$) is linear. The slope of the KS-relation can be anywhere between 1.0 and 1.7, shows substantial scatter for modest samples and steepens for an increasing range in specific star formation rate of the sample and increasing redshift.

Given that submillimeter detections of dust emission with the ALMA telescope are substantially more efficient than the detection of CO line emission, especially at $z > 1$, we have tested the reliability of single-frequency band continuum measurements of molecular gas masses across the parameter space sampled by our data. We find that without applying individual Planck-corrections owing to the variation of T_{dust} , single band measurements will be affected by large systematic trends. These trends can be corrected for by the empirical scaling relation we have proposed in Table 5, or by two-band ALMA measurements, which however require relatively long integrations and thus much of the initial advantage of the continuum technique (relative to the dust technique) is lost.

Acknowledgements

We are grateful to the staff of the IRAM facilities for the continuing excellent support of the large CO survey programs we have been analysing in this paper. We also thank

Albrecht Poglitsch and Matt Griffin, the PACS and SPIRE teams and ESA for their excellent work on the Herschel instruments and mission. We acknowledge Guinevere Kauffmann for her leadership in bringing the COLDGASS program to fruition. We thank Alain Omont for his support of the PHIBSS programs at IRAM.

References

- Abdo A. A., Ackermann, M., Ajello, M., et al. 2010, ApJ, 710, 133
- Adelberger, K. L., Steidel, C. C., Shapley, A. E., et al. 2004, ApJ, 607, 226
- Aravena, M., Hodge, J. A., Wagg, J., et al. 2014, MNRAS, 442, 558
- Armus, L., Mazzarella, J. M., Evans, A. S., et al. 2009, PASP, 121, 559
- Asplund, M., Grevesse, N., Sauval, A. J., Allende Prieto, C. & Kiselman, D. 2004, A&A, 417, 751
- Bauermeister, A., Blitz, L., Bolatto, A., et al. 2013, ApJ, 763, 64
- Berta, S., Magnelli, B., Lutz, D. et al. 2010, A&A 518, L30
- Bethermin, M., Daddi, E., Magdis, G. et al. 2014, submitted to ApJ
- Bianchi, S. 2013, A&A, 552, 89
- Bigiel, F., Leroy, A., Walter, F., et al. 2008, AJ, 136, 2846
- Bigiel, F., Leroy, A. K., Walter, F., et al. 2011, ApJ, 730, 13
- Bolatto, A. D., Leroy, A. K., Rosolowsky, E., Walter, F., & Blitz, L. 2008, ApJ, 686, 948
- Bolatto, A. D., Wolfire, M., & Leroy, A. K. 2013, ARA&A, 51, 207
- Bothwell, M. S., Smail, I., Chapman, S. C., et al. 2013, MNRAS, 429, 3047
- Bouché, N., Dekel, A., Genzel, R., et al. 2010, ApJ, 718, 1001
- Brammer, G.B., van Dokkum, P.G., Franx, M. et al. 2012 ApJS 200, 13
- Brinchmann, J., Charlot, S., White, S. D. M., et al. 2004, MNRAS, 351, 1151
- Bruzual, G. & Charlot, S. 2003, MNRAS, 344, 1000
- Bullock, J.S., Kolatt, T.S., Sigad, Y. et al. 2001a, MNRAS 321, 559

- Bullock, J.S., Dekel, A., Kolatt, T.S., Kravtsov, A.V., Klypin, A.A., Porciani, C. & Primack, J.R. 2001b, ApJ 555, 240
- Calzetti, D., Armus, L., Bohlin, R. C., et al. 2000, ApJ, 533, 682
- Carilli, C. L. & Walter, F. 2013, ARA&A, 51, 105
- Chabrier, G. 2003, PASP, 115, 763
- Combes, F., García-Burillo, S., Braine, J., Schinnerer, E., Walter, F. & Colina, L. 2011, A&A, 528, 124
- Combes, F., García-Burillo, S., Braine, J., et al. 2013, A&A, 550, 41
- Conroy, C., & Wechsler, R. H. 2009, ApJ, 696, 620
- Cooper, M.C., Griffith, R.L., Newman, J.A. 2012, MNRAS, 419, 3018
- Cox, P. 2011, IRAM Annual Reports,
<http://iram.fr/IRAMFR/ARN/AnnualReports/Years.html>
- Daddi, E., Bournaud, F., Walter, F., et al. 2010a, ApJ, 713, 686
- Daddi, E., Dannerbauer, H., Elbaz, D., et al. 2008, ApJL, 673, 21
- Daddi, E., Dickinson, M., Morrison, G., et al. 2007, ApJ, 670, 156
- Daddi, E., Elbaz, D., Walter, F., et al. 2010b, ApJL, 714, L118
- Dale, D. A. & Helou, G. 2002, ApJ, 576, 159
- Dame, T. M., Hartmann, D., & Thaddeus, P. 2001, ApJ, 547, 792
- Dannerbauer, H., Daddi, E., Riechers, D. A., et al. 2009, ApJL, 698, L178
- Danovich, M., Dekel, A., Hahn, O., Ceverino, D. & Primack, J.S. 2014, astro-ph 1407.7129
- Davé, R., Finlator, K., & Oppenheimer, B. D. 2011, MNRAS, 416, 1354
- Davé, R., Finlator, K., & Oppenheimer, B. D. 2012, MNRAS, 421, 98

Davis, M., Guhathakurta, P., Konidaris, N. P., et al. 2007, *ApJL*, 660, L1

Dickman, R. L., Snell, R. L., & Schloerb, F. P. 1986, *ApJ*, 309, 326

Dobbs, C. L., Burkert, A. & Pringle, J. E. 2011, *MNRAS*, 413, 2935

Dobbs, C. L. & Pringle, J. E. 2013, *MNRAS*, 432, 653

Downes, D. & Solomon, P. M. 1998, *ApJ*, 507, 615

Draine, B. T., Dale, D. A., Bendo, G., et al. 2007, *ApJ*, 663, 866

Draine, B. T. & Li, A. 2007, *ApJ*, 657, 810

Dutton, A.A., van den Bosch, F., Faber, S.M. et al. 2011, *MNRAS* 410, 1660

Elbaz, D., Daddi, E., Le Borgne, D., et al. 2007, *A&A*, 468, 33

Elbaz, D., Dickinson, M., Hwang, H. S., et al. 2011, *A&A*, 533, 119

Elmegreen, B.G. 1997, *Rev.Mexicana Astron. Astrofis. Conf. Ser.* 6, 165

Erb, D. K., Shapley, A. E., Pettini, M., et al. 2006, *ApJ*, 644, 813

Feldmann, R., Gnedin, N. Y. & Kravtsov, A. V. 2012a, *ApJ*, 747, 124

Feldmann, R., Gnedin, N. Y. & Kravtsov, A. V. 2012b, *ApJ*, 758, 127

Förster Schreiber, N. M., Genzel, R., Bouché, N., et al. 2009, *ApJ*, 706, 1364

Fu, J., Kauffmann, G., Li, C., & Guo, Q. 2012, *MNRAS*, 424, 2701

Gao, Y. & Solomon, P. M. 2004, *ApJ*, 606, 271

Genzel, R., Lutz, D., Sturm, E. et al. 1998, *ApJ*, 498, 579

Genzel, R., Tacconi, L. J., Gracia-Carpio, J., et al. 2010, *MNRAS*, 407, 2091

Genzel, R., Tacconi, L. J., Combes, F., et al. 2012, *ApJ*, 746, 69

Genzel, R., Förster Schreiber, N.M., Lang, P. et al. 2014, *ApJ*, 785, 75

Giavalisco, M., Ferguson, H. C., Koekemoer, A. M., et al. 2004, *ApJ*, 600, 93

Glover, S. C. O. & Clark, P. C. 2012, *MNRAS*, 421, 9

Garcia-Burillo, S., Usero, A., Alonso-Herrero, A., Gracia-Carpio, J., Pereira-Santaella, M., Colina, L., Planesas, P. & Arribas, S. 2012, A&A, 539, 8

Gracia-Carpio, J., Garcia-Burillo, S. Planesas, P., Fuente, A. & Usero, A. 2008, A&A 479, 703

Gracia-Carpio, J. 2009, PhD thesis, University of Madrid

Grenier, I. A., Casandjian, J.-M., & Terrier, R. 2005, Sci, 307, 1292

Greve, T., Bertoldi, F., Smail, I., et al. 2005, MNRAS, 359, 1165

Grogin, N.A., Kocevski, D.D., Faber, S.M. et al. 2011, ApJS, 197, 35

Guilloteau, S., Delannoy, J., Downes, D., et al. 1992, A&A, 262, 624

Heiderman, A., Evans, N. J. II, Allen, L. E., Huard, T., & Heyer, M. 2010, ApJ, 723, 1019

Huang, M.-L. & Kauffmann, G. 2014, MNRAS, submitted / arXiv:1404.7138

Iverson, R. J., Papadopoulos, P. P., Smail, I., et al. 2011, MNRAS, 412, 1913

Juneau, S., Narayanan, D. T., Moustakas, J., et al. 2009, 707, 1217

Karim, A., Schinnerer, E., Martinez-Sansigre, A., et al. 2011, ApJ, 730, 61

Kennicutt, R. C., Jr. 1989, ApJ, 344, 685

Kennicutt, R. C., Jr. 1998, ApJ 498, 541

Kennicutt, R. C., Jr., Calzetti, D., Walter, F., et al. 2007, ApJ, 671, 333

Kennicutt, R.C., Jr. & Evans, N. 2012, ARA&A 50, 531

Koekemoer, A.M., Faber, S.M., Ferguson, H.C. et al. 2011, ApJS 197, 36

Kong, X. et al. 2006 ApJ 638, 72

Krumholz, M.R. & McKee, C.F. 2005, ApJ 630, 250

Krumholz, M. R., Leroy, A. K., & McKee, C. F. 2011, ApJ, 731, 25

Krumholz, M.R., Dekel, A. & McKee, C.F. 2012, ApJ, 745, 69

Lada, C. J., Forbrich, J., Lombardi, M., & Alves, J. F. 2012, ApJ, 745, 190

Lagos, C. D. P., Baugh, C. M., Lacey, C. G., et al. 2011, MNRAS, 418, 1649

Lagos, C. D. P., Bayet, E., Baugh, C. M., et al. 2012, MNRAS, 426, 2142

Leroy, A. K., Bolatto, A., Gordon, K., et al. 2011, ApJ, 737, 12

Leroy, A. K., Walter, F., Brinks, E., et al. 2008, AJ, 136, 2782

Leroy, A. K., Walter, F., Sandstrom, K., et al. 2013, AJ, 146, 19

Li, A. & Draine, B.T. 2001, ApJ, 554, 778

Lilly, S.J., LeFevre, O., Renzini, A. et al. 2007, ApJS 172, 70

Lilly, S.J., LeBrun, V., Maier, C, et al. 2009, ApJS 184, 218

Lilly, S. J., Carollo, C. M., Pipino, A., Renzini, A., & Peng, Y. 2013, ApJ, 772, 119

Lutz, D., Poglitsch, A., Altieri, B., et al. 2011, A&A, 532, 90

Magdis, G. E., Daddi, E., Béthermin, M., et al. 2012b, ApJ, 760, 6

Magdis, G. E., Daddi, E., Sargent, M., et al. 2012a, ApJ, 758, 9

Magnelli, B., Saintonge, A., Lutz, D., et al. 2012, A&A, 548, 22

Magnelli, B., Lutz, D., Saintonge, A., et al. 2014, A&A, 561, 86

Maiolino, R., Nagao, T., Grazian, A., et al. 2008, A&A, 488, 463

Martig, M., Bournaud, F., Teyssier, R. & Dekel, A. 2009, ApJ, 707, 250

McKee, C. F. & Ostriker, E. C. 2007, ARA&A 45, 565

Mo, H.J., Mao, S. & White, S.D.M. 1998, MNRAS 295, 319

Narayanan, D., Krumholz, M., Ostriker, E. C., & Hernquist, L. 2011, MNRAS, 418, 664

Narayanan, D., Krumholz, M., Ostriker, E. C., & Hernquist, L. 2012, MNRAS, 421, 3127

Newman, J.A., Cooper, M.C., Davis, M. et al. 2013, ApJS, 208, 5

Newman, S. F., Genzel, R., Förster Schreiber, N. M., et al. 2013, *ApJ*, 767, 104

Noeske, K. G., Weiner, B. J., Faber, S. M., et al. 2007, *ApJL*, 660, L43

Oliver, S. J., Bock, J., Altieri, B., et al. 2012, *MNRAS*, 424, 1614

Ostriker, E. C., McKee, C. F., & Leroy, A. K. 2010, *ApJ*, 721, 975

Pannella, M., Carilli, C. L., Daddi, E., et al. 2009, *ApJL*, 698, L116

Peng, Y., Lilly, S. J., Kovač, K., et al. 2010, *ApJ*, 721, 193

Peng, Y. & Maiolino, R. 2014, *MNRAS*, 438, 262

Pettini, M. & Pagel, B. E. J. 2004, *MNRAS*, 348, 59

Planck Collaboration 2011a, *A&A*, 536, A21

Planck Collaboration 2011b, *A&A*, 536, A25

Riechers, D. A., Carilli, C. L., Walter, F., & Momjian, E. 2010, *ApJL*, 724, L153

Riechers, D. A. 2013, *ApJ*, 765, 31

Rodighiero, G., Cimatti, A., Gruppioni, C., et al. 2010, *A&A*, 518, 25

Rodighiero, G., Daddi, E., Baronchelli, I., et al. 2011, *ApJ*, 739, 40

Saintonge, A., Kauffmann, G., Kramer, C., et al. 2011a, *MNRAS*, 415, 32

Saintonge, A., Kauffmann, G., Wang, J., et al. 2011b, *MNRAS*, 415, 61

Saintonge, A., Tacconi, L. J., Fabello, S., et al. 2012, *ApJ*, 758, 73

Saintonge, A., Lutz, D., Genzel, R., et al. 2013, *ApJ*, 778, 2

Salmi, F., Daddi, E., Elbaz, D., et al. 2012, *ApJ*, 754, 14

Santini, P., Maiolino, R., Magnelli, B., et al. 2014, *A&A*, 562, 30

Sargent, M.T., Béthermin, M., Daddi, E., & Elbaz, D. 2012, *ApJ*, 747, 31

Schiminovich, D., Wyder, T. K., Martin, D. C., et al. 2007, *ApJS*, 173, 315

Schruba, A., Leroy, A. K., Walter, F., et al. 2011, *AJ*, 142, 37

Scoville, N. Z. 2013 in *Secular Evolution of Galaxies*, ed. J. Falcón-Barroso and J. H. Knapen (Cambridge, UK: Cambridge University Press), 491

Scoville, N. Z., Yun, M. S. & Bryant, P. M 1997, *ApJ*, 484, 702

Scoville, N., Aussel, H., Sheth, K., et al. 2014, *ApJ*, 783, 84

Shapiro, K. L., Genzel, R., Förster Schreiber, N. M., et al. 2008, *ApJ*, 682, 231

Silk, J. 1997, *ApJ* 481, 702

Skelton, R.E., Whitaker, K.E., Momcheva, I.G. et al. 2014 *ArXiv*1403.3689

Solomon, P. M., Downes, D., Radford, S. J. E., & Barrett, J. W. 1997, *ApJ*, 478, 144

Solomon, P. M., Rivolo, A. R., Barrett, J., & Yahil, A. 1987, *ApJ*, 319, 730

Solomon, P. M. & Sage, L. J. 1988, *ApJ*, 334, 613

Somerville, R.S., Barden, M., Rix, H.-W. et al. 2008 *ApJ* 672, 776

Steidel, C. C., Shapley, A. E., Pettini, M., et al. 2004, *ApJ*, 604, 534

Strong, A. W. & Mattox, J. R. 1996, *A&A*, 308, L21

Tacconi, L. J., Genzel, R., Neri, R., et al. 2010, *Natur*, 463, 781

Tacconi, L. J., Genzel, R., Smail, I., et al. 2008, *ApJ*, 680, 246

Tacconi, L. J., Neri, R., Chapman, S. C., et al. 2006, *ApJ*, 640, 228

Tacconi, L. J., Neri, R., Genzel, R., et al. 2013, *ApJ*, 768, 74

van der Wel, A., Franx, M., van Dokkum, P.G. et al. 2014, *ApJ* 788, 28

Weiss, A., Downes, D., Walter, F., & Henkel, C. 2007, in *ASP Conf. Ser. 375, From Z-Machines to ALMA: (Sub)Millimeter Spectroscopy of Galaxies*, ed. A. J. Baker, J. Glenn, A. I. Harris, J. G. Mangum, & M. S. Yun (San Francisco, CA: ASP), 25

Whitaker, K. E., van Dokkum, P. G., Brammer, G., & Franx, M. 2012, *ApJ*, 754, 29L

Whitaker, K.E., Franx, M., Leja, J. et al. 2014, *arXiv*1407.1843

Wisnioski, E., Förster Schreiber, N. M., Wuyts, S., et al. 2014, ApJ, submitted

Wolfire, M. G., Hollenbach, D. & McKee, C. F. 2010, ApJ, 716, 1191

Wuyts, S., Förster Schreiber, N. M., Lutz, D., et al. 2011a, ApJ, 738, 106

Wuyts, S., Förster Schreiber, N. M., van der Wel, A., et al. 2011b, ApJ, 742, 96

Wuyts, E., Kurk, J., Förster Schreiber, N. M., et al. 2014, ApJ, 789, 40

Young, J. S. & Scoville, N. Z. 1991, ARA&A, 29, 581

Zahid, H. J., Kashino, D., Silverman, J. D., et al. 2014, ApJ, in press / arXiv:1310.4950

Figures

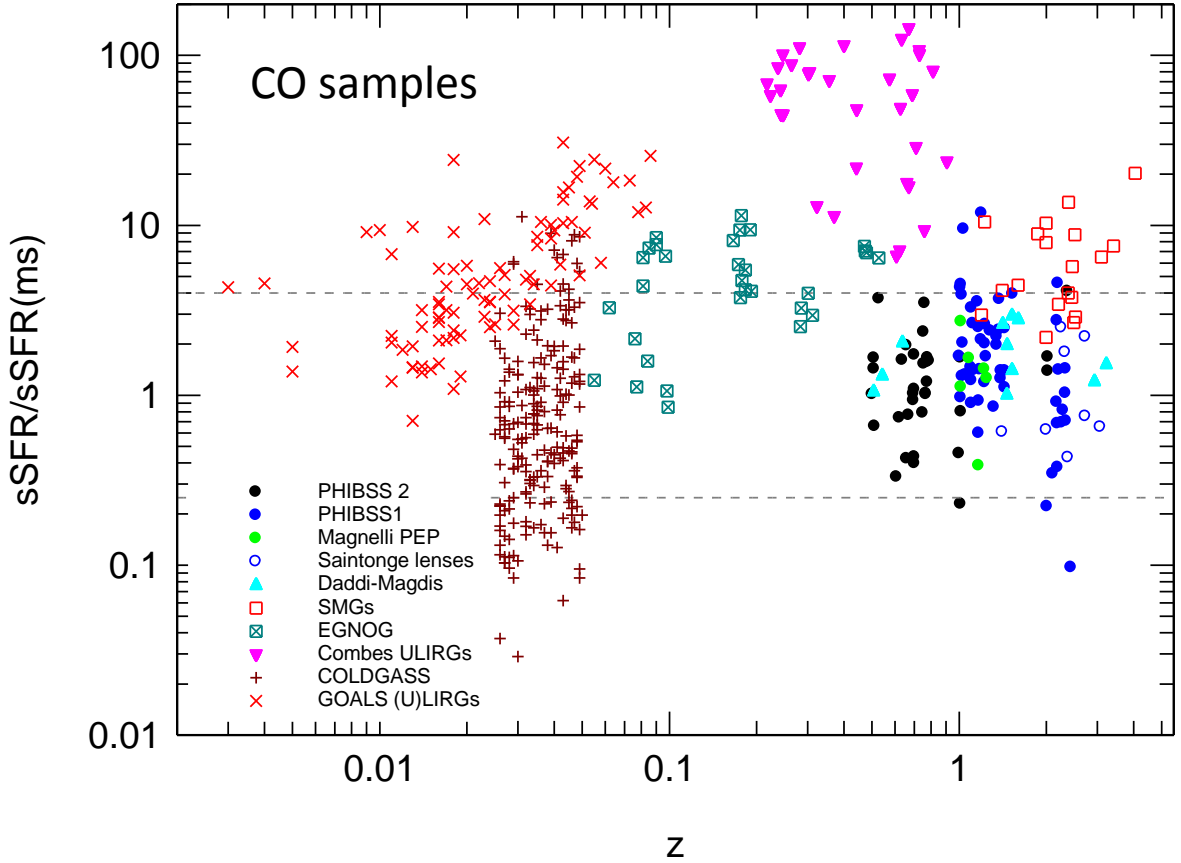


Figure 1: Distribution in the redshift –specific star formation rate plane of the 500 SFGs with integrated CO (1-0, 2-1, 3-2 and 4-3) flux measurements used in this paper. The various symbols denote the different publications from which these measurements were taken, as discussed in the text (section 2.1, Table 1). The vertical axis is normalized so that the mid-line of the star formation sequence at each redshift is at unity, using the scaling relations $sSFR(ms, z, M_*)$ from equation (1) (Whitaker et al. 2012). Horizontal

dashed lines mark the upper and lower range of the main sequence, ± 0.6 dex from that mid-line.

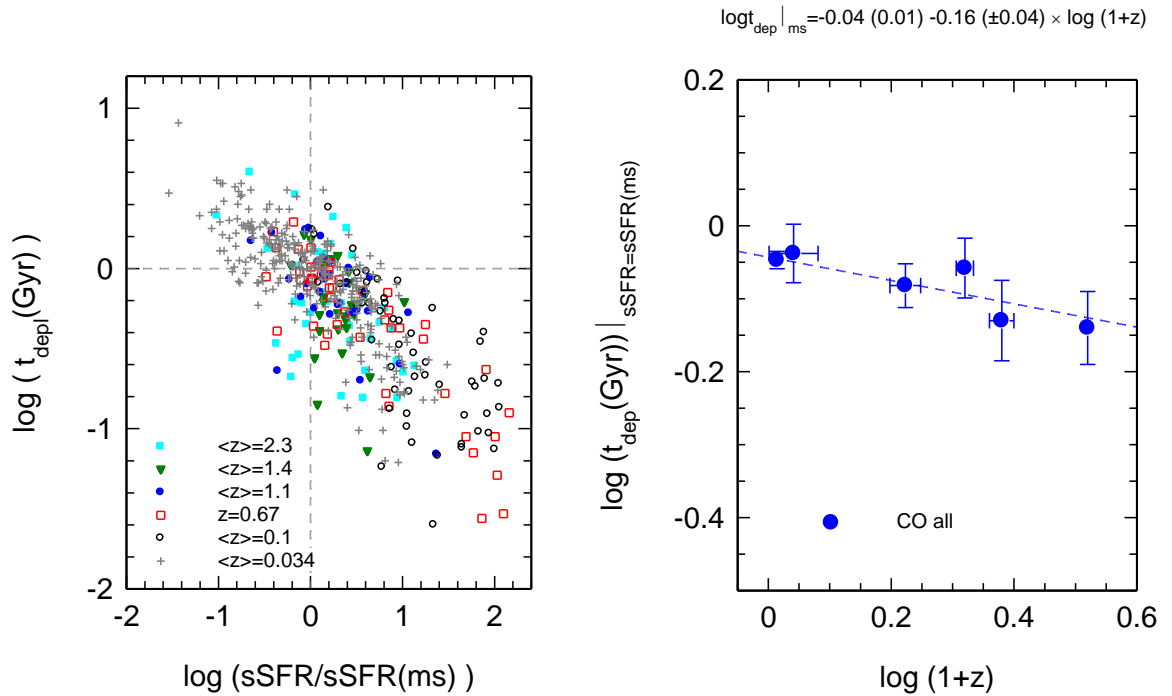


Figure 2: left panel: dependence of the CO-based molecular gas depletion time scale, $t_{\text{dep}} = \alpha_{0J} L_{\text{CO}} / \text{SFR}$ (equations (4) & (8)) as a function of specific star formation rate, normalized to the main-sequence mid-line value at each redshift (from equation (1), Whitaker et al. 2012), for the 500 galaxies from Figure 1 with integrated CO measurements, binned in 6 redshift ranges from $z=0$ to 2.3. Right panel: dependence of the depletion time at the main-sequence mid-line on redshift, obtained from the zero-

point offsets in slope -0.46 linear fits in the log-log distributions in the left panel in each redshift bin. The best linear fit has a slope of -0.16 (dashed line).

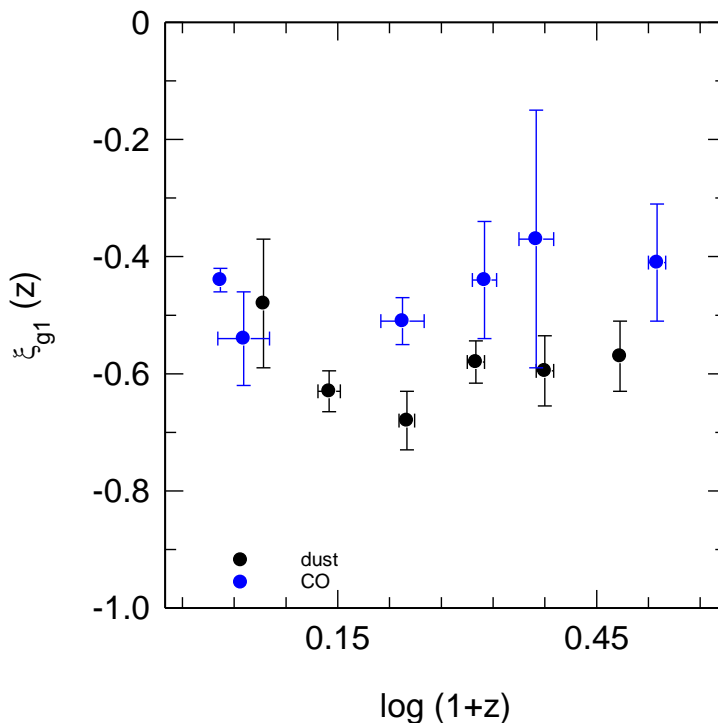


Figure 3. Slopes $\xi_{g1}(z) = d \log t_{depl}(z) / d \log (sSFR/sSFR(ms,z,M_*))$ as a function of $\log(1+z)$ for the CO data in the 6 redshift bins at $\langle z \rangle \sim 0, 0.1, 0.67, 1, 1.4$ and 2.3 (Table 1) (filled blue circles), and for the Herschel dust data in the 6 redshift binds at $\langle z \rangle \sim 0.1, 0.35, 0.65, 1, 1.45$ and 2 (Table 2) (filled black circles). Error bars are 1σ . A weighted power law fit to these data yields a slope of $d\xi_{g1}(z)/d \log(1+z) = -0.08 (\pm 0.13, 1\sigma)$ for the CO data, and $d\xi_{g1}(z)/d \log(1+z) = +0.13 (\pm 0.18)$ for the dust data. The best fitting constant (z) slopes ξ_{g1} are -0.46 and -0.59 for the CO and dust data.

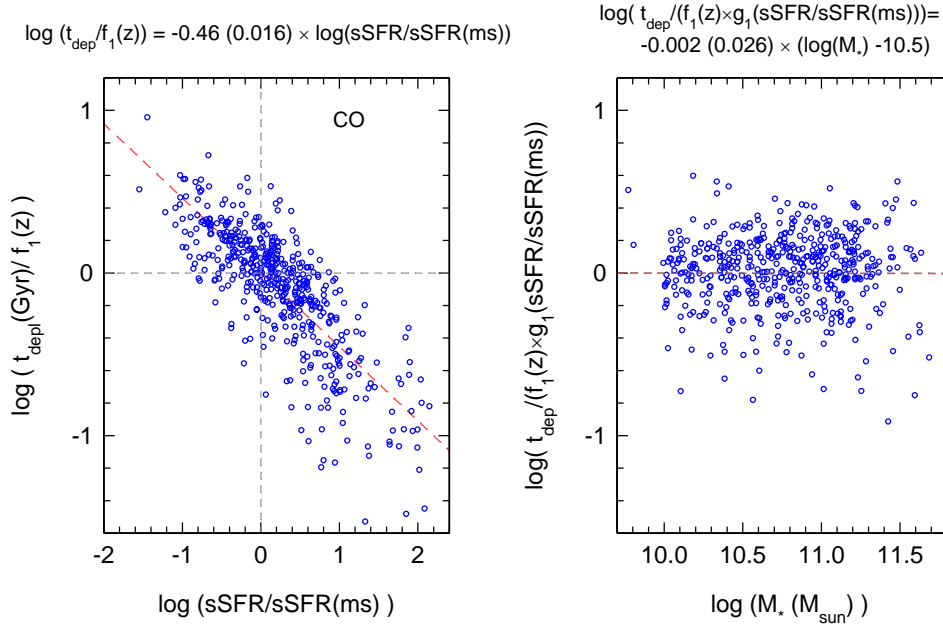


Figure 4: left panel: dependence of CO-based depletion time scale (equations (4) & (8)) on specific star formation rate normalized to the mid-line of main-sequence at each redshift (equation (1) and Figure 3, Whitaker et al. 2012), after removing the redshift dependence with the fitting function $f_I(z) = 10^{-0.04 - 0.16 \times \log(1+z)}$ obtained from the right panel of Figure 3. The red-dashed line is the best linear fit to the log-log distribution of all 500 SFGs and has a slope of -0.46. The residuals have a scatter of ± 0.23 dex. Right panel: dependence of CO-based depletion time scale on stellar mass, after removing also the specific star formation rate dependence with the fitting function $g_I(\text{sSFR}/\text{sSFR}(\text{ms}, z, M_*)) = 10^{-0.46 \times \log(\text{sSFR}/\text{sSFR}(\text{ms}, z, M_*))}$ obtained from the left panel of the Figure.

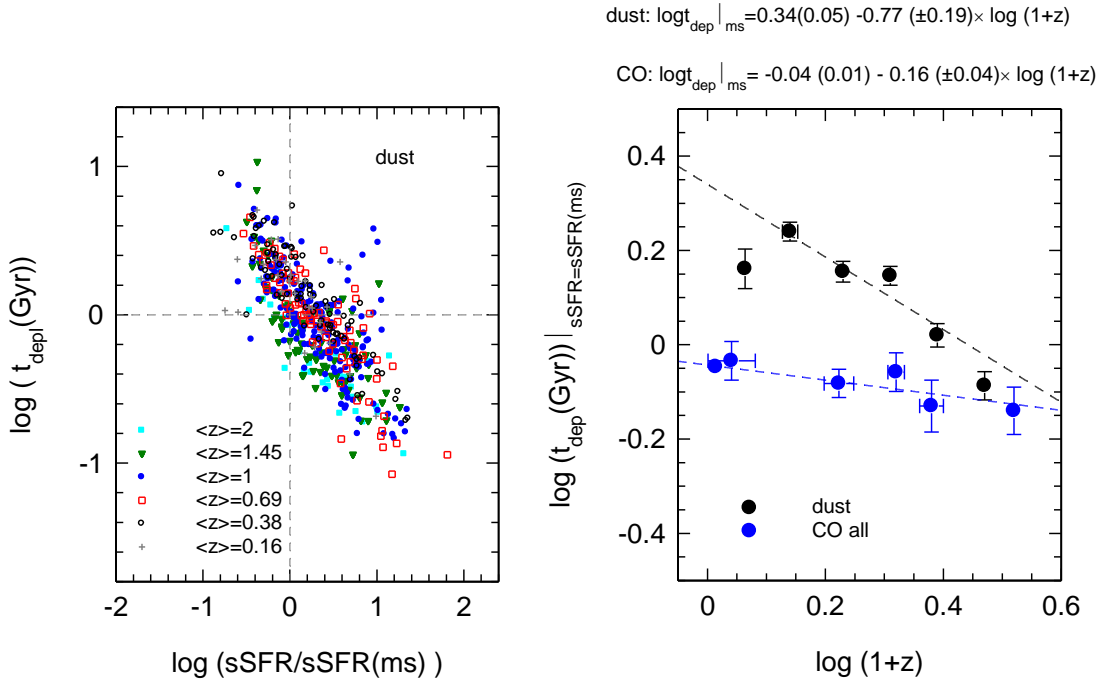


Figure 5: left panel: dependence of the dust-based molecular gas depletion time scale, $t_{\text{dep}} = M_{\text{molgas}} (M_{\text{dust}}) / \text{SFR}$ (equations (9) & (10)) as a function of specific star formation rate, normalized to the main-sequence mid-line value at each redshift (from equation (1), Whitaker et al. 2012), for the 512 PACS-SPIRE stacks from Magnelli et al. (2014), binned in 6 redshift ranges from $z=0.1$ to 2. Right panel: dependence of the dust-based depletion time (black circles) at the main-sequence mid-line on redshift, obtained from the zero-point offsets in slope -0.59 linear fits in the log-log distributions in the left panel in each redshift bin. The best linear fit has a slope of -0.77 (black dashed line). For comparison the filled blue circles and blue dashed line denote the CO-based data from Figure 3.

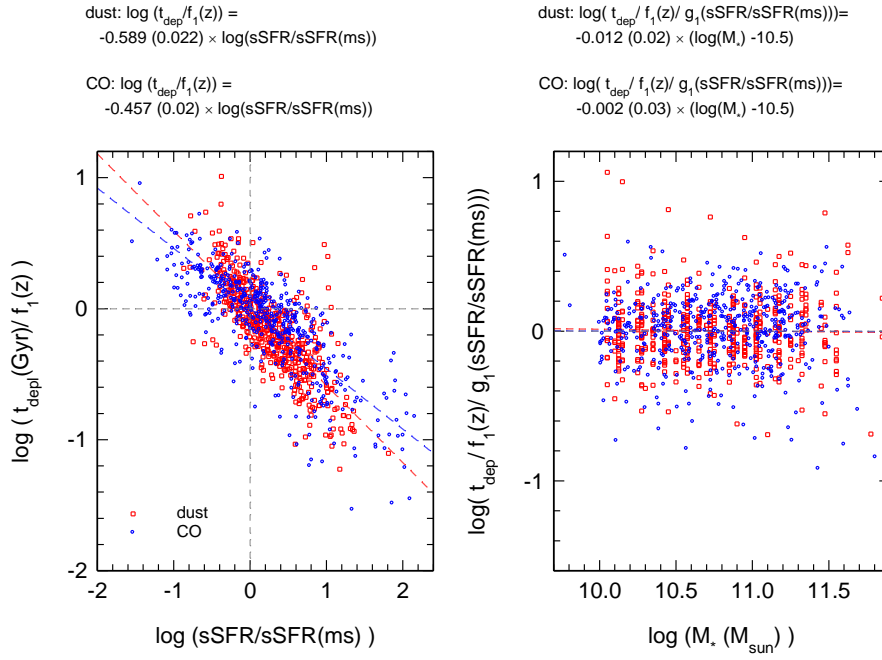


Figure 6: left panel: dependence of CO-based (blue) and dust-based (red) depletion times on specific star formation rate normalized to the mid-line of main-sequence at each redshift (equation (1), Whitaker et al. 2012), after removing the redshift dependences with the fitting functions $f_1(z)$ given in the right panels of Figure 3 and Figure 5. The blue- and red-dashed lines are the best linear fits to the log-log distributions of all 500 CO SFGs and all 512 Herschel stacks. Right panel: dependence of CO-based (blue) and dust-based (red) depletion times on stellar mass, after removing also the specific star formation rate dependence with the fitting function

$$g_1(\text{sSFR}/\text{sSFR}(m_s, z, M_*)) = 10^{-0.46 \times \log(\text{sSFR}/\text{sSFR}(m_s, z, M_*))} \text{ for CO and}$$

$$g_1(\text{sSFR}/\text{sSFR}(m_s, z, M_*)) = 10^{-0.589 \times \log(\text{sSFR}/\text{sSFR}(m_s, z, M_*))} \text{ for the dust data, as obtained from the}$$

left panel of the Figure. The residuals from the best power law fits are ± 0.23 dex for both the CO- and dust-data.

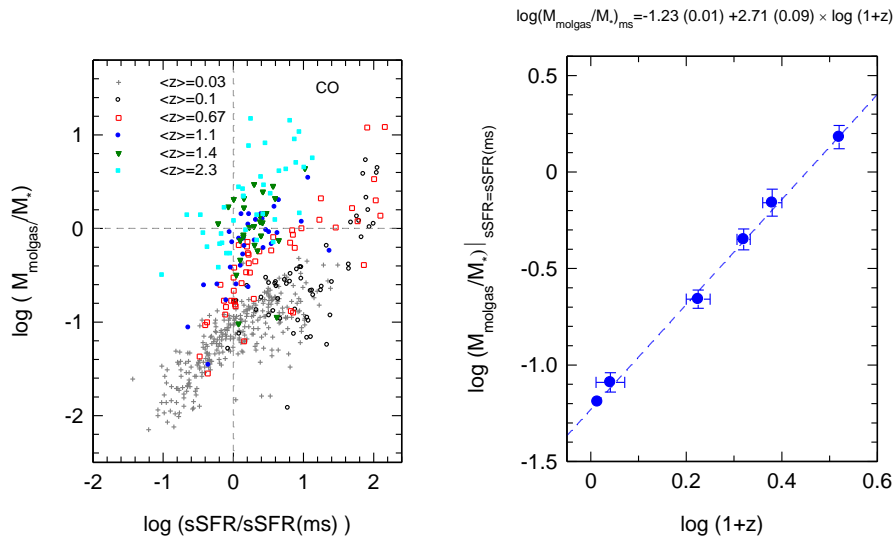


Figure 7. left panel: dependence of the CO-based molecular gas mass to stellar mass ratio, $M_{\text{molgas}}/M_* = \alpha_{0J} L_{\text{CO}J}'/M_*$ (equations (4) & (8)) as a function of specific star formation rate, normalized to the main-sequence mid-line value at each redshift (from equation (1), Whitaker et al. 2012), for the 500 galaxies from Figure 1 with integrated CO measurements, binned in 6 redshift ranges from $z=0$ to 3.4. Right panel: dependence of the CO-based molecular gas mass to stellar mass ratio at the main-sequence mid-line on redshift, obtained from the zero-point offsets in slope +0.51 linear fits in the log-log distributions in the left panel in each redshift bin. The best linear fit has a slope of 2.71 (dashed line).

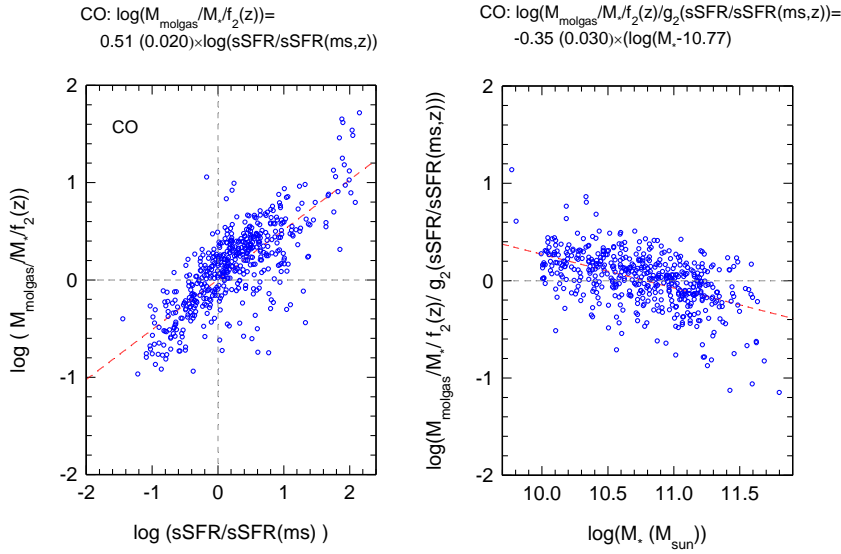


Figure 8: left panel: dependence of CO-based molecular gas mass to stellar mass ratio, $M_{\text{molgas}}/M_* = \alpha_0 J L_{\text{CO}J}'/M_*$ (equations (4) & (8)) on specific star formation rate normalized to the mid-line of main-sequence at each redshift (equation (1), Whitaker et al. 2012), after removing the steep redshift dependence with the fitting function $f_2(z) = 10^{1.23+2.71 \times \log(1+z)}$ obtained from the right panel of Figure 7. The red-dashed line is the best linear fit to the log-log distribution of all 500 SFGs and has a slope of 0.51. Right panel: dependence of CO-based gas mass to stellar mass ratio on stellar mass, after removing also the specific star formation rate dependence with the fitting function $g_2(\text{sSFR}/\text{sSFR}(ms,z,M_*)) = 10^{0.51 \times \log(\text{sSFR}/\text{sSFR}(ms,z,M_*))}$ obtained from the left panel of the Figure. The resulting best linear fit has a slope of -0.35.

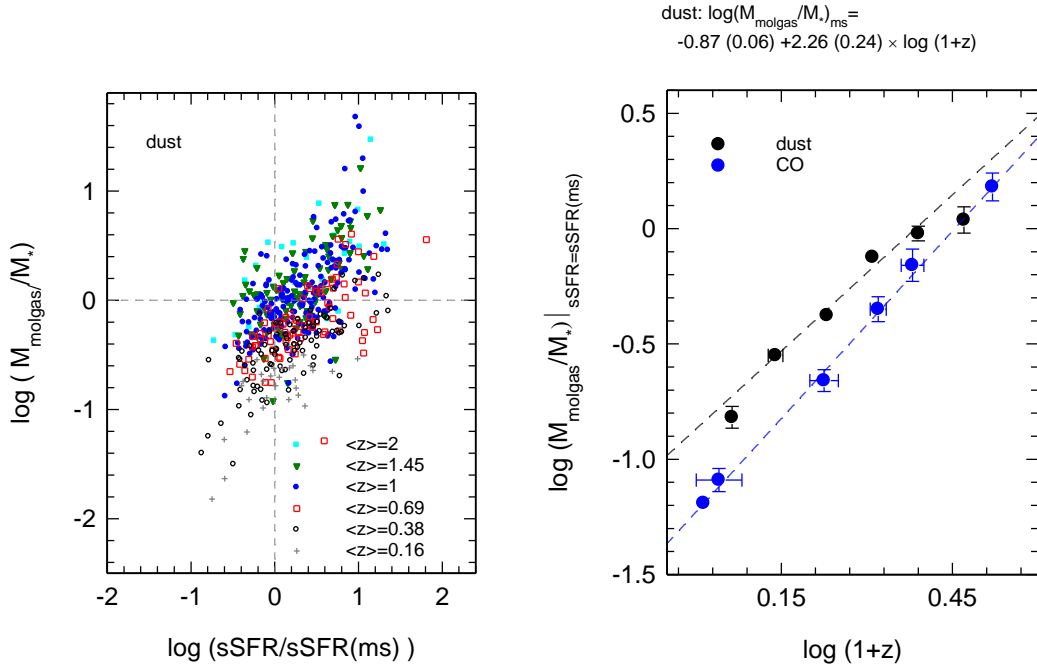


Figure 9: left panel: dependence of the dust-based molecular gas mass to stellar mass ratio, $M_{\text{molgas}}/M_* = M_{\text{molgas}}(M_{\text{dust}})/M_*$ (equations (9) & (10)) as a function of specific star formation rate, normalized to the main-sequence mid-line value at each redshift (from equation (1), Whitaker et al. 2012), for the 512 PACS-SPIRE stacks from Magnelli et al. (2014), binned in 6 redshift ranges from $z=0.1$ to 2. Right panel: dependence of the dust-based molecular gas mass to stellar mass ratio (black circles) at the main-sequence mid-line on redshift, obtained from the zero-point offsets in slope 0.5 linear fits in the log-log distributions in the left panel in each redshift bin. The best linear fit has a slope of 2.26 (black dashed line). For comparison the filled blue circles and blue dashed line denote the CO-based data from Figure 8.

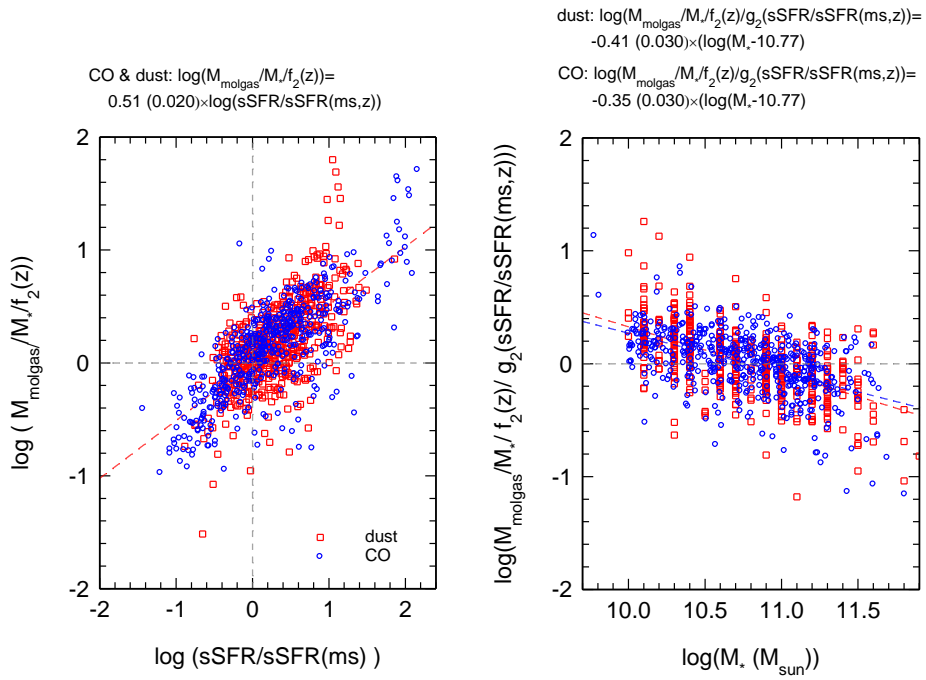


Figure 10: left panel: dependence of CO-based (blue) and dust-based (red) molecular gas mass to stellar mass ratios on specific star formation rate normalized to the mid-line of main-sequence at each redshift (equation (1), Whitaker et al. 2012), after removing the redshift dependences with the fitting functions $f_2(z)$ given in the right panels of Figure 7 and Figure 9. The blue- and red-dashed lines are the best linear fits to the log-log distributions of all 500 CO SFGs and all 512 Herschel stacks. Right panel: dependence of CO-based (blue) and dust-based (red) molecular gas to stellar mass ratio, after removing also the specific star formation rate dependence with the fitting function $g_2(\text{sSFR}/\text{sSFR}(\text{ms}, z, M_*)) = 10^{-0.51 \times \log(\text{sSFR}/\text{sSFR}(\text{ms}, z, M_*))}$ for CO and for the dust data, as obtained from the left panel of the Figure.

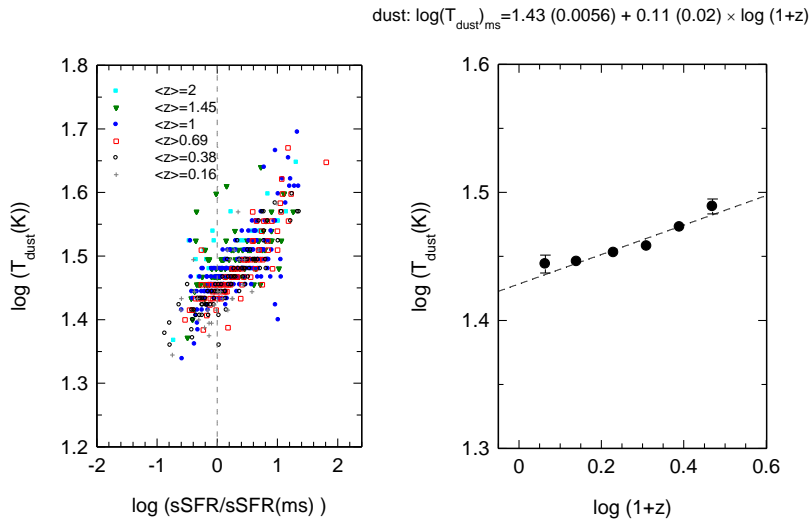


Figure 11: left panel: dependence of the dust temperature as a function of specific star formation rate, normalized to the main-sequence mid-line value at each redshift (from equation (1), Whitaker et al. 2012), for the 512 PACS-SPIRE stacks from Magnelli et al. (2014), binned in 6 redshift ranges from $z=0.1$ to 2. Right panel: dependence of the dust temperature at the main-sequence mid-line on redshift, obtained from the zero-point offsets in slope 0.086 linear fits in the log-log distributions in the left panel in each redshift bin. The best linear fit has a slope of 0.11 (black dashed line).

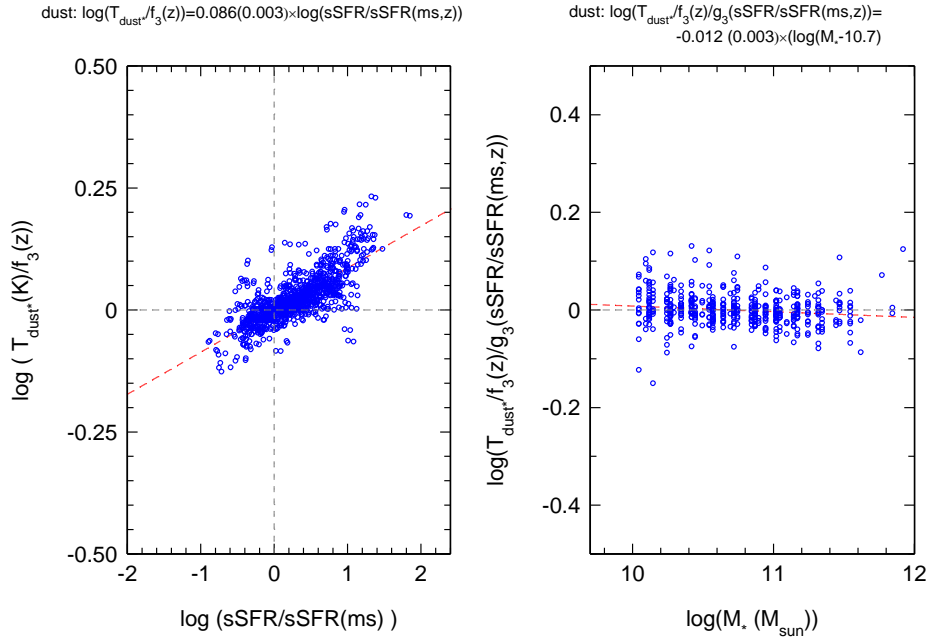


Figure 12: left panel: dependence of dust temperature on specific star formation rate normalized to the mid-line of main-sequence at each redshift (equation (1), Whitaker et al. 2012), after removing the redshift dependence with the fitting function $f_3(z) = 10^{1.43 + 0.11 \times \log(1+z)}$ obtained from the right panel of Figure 7. The red-dashed line is the best linear fit to the log-log distribution of all 512 stacks and has a slope of $0.086 (\pm 0.003)$. Right panel: dependence of dust temperature on stellar mass, after removing also the specific star formation rate dependence with the fitting function $g_3(\text{sSFR}/\text{sSFR}(\text{ms}, z, M_*)) = 10^{0.064 \times \log(\text{sSFR}/\text{sSFR}(\text{ms}, z, M_*))}$ obtained from the left panel of the Figure. The resulting best linear fit has a slope of -0.012 .

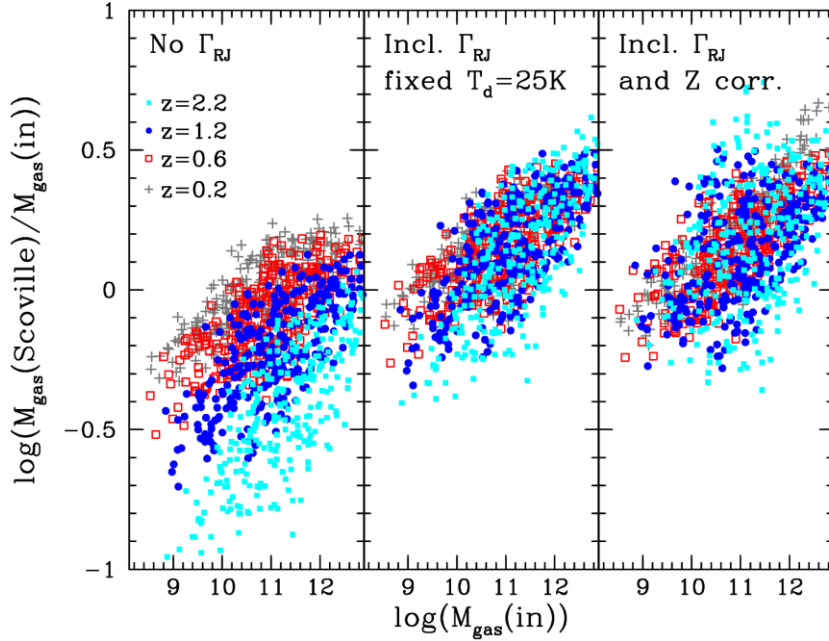


Figure 13: Gas masses inferred from single frequency photometry (ALMA band 7, 350 GHz) in the Rayleigh-Jeans-tail of the dust SED (for assumed $T_{\text{dust}}=25$ K= const: the ‘Rayleigh-Jeans tail’ method, see text), relative to the “true” input gas masses. For this purpose we used the scaling relations in Tables 4 to 5 to compute input gas masses as a function of redshift, specific star formation rate offset and stellar mass ($\log(M_*/M_\odot)=10$ -11.5), on the same grid points as in Magnelli et al. (2014, same color coding as in Figures 5, 9 and 11). The left panel shows the performance of the ‘Rayleigh-Jeans tail’ method (see Scoville 2013, Scoville et al. 2014) for $T_{\text{dust}}=\text{const}$ in the Rayleigh-Jeans approximation (instead of applying a Planck correction with a dust temperature that is varying according to the scaling relations in Table 5), and without the metallicity dependent dust to gas ratio correction in equation (10). The central panel shows the performance of the ‘Rayleigh-Jeans tail’ method if a constant Planck correction (for $T_{\text{dust}}=\text{const}=25$ K) is applied to all data but again (as in the left panel) the metallicity

dependent gas to dust ratio correction is omitted. The right panel still uses a constant Planck correction but now the metallicity dependent dust to gas ratio correction in equation (10) is applied.

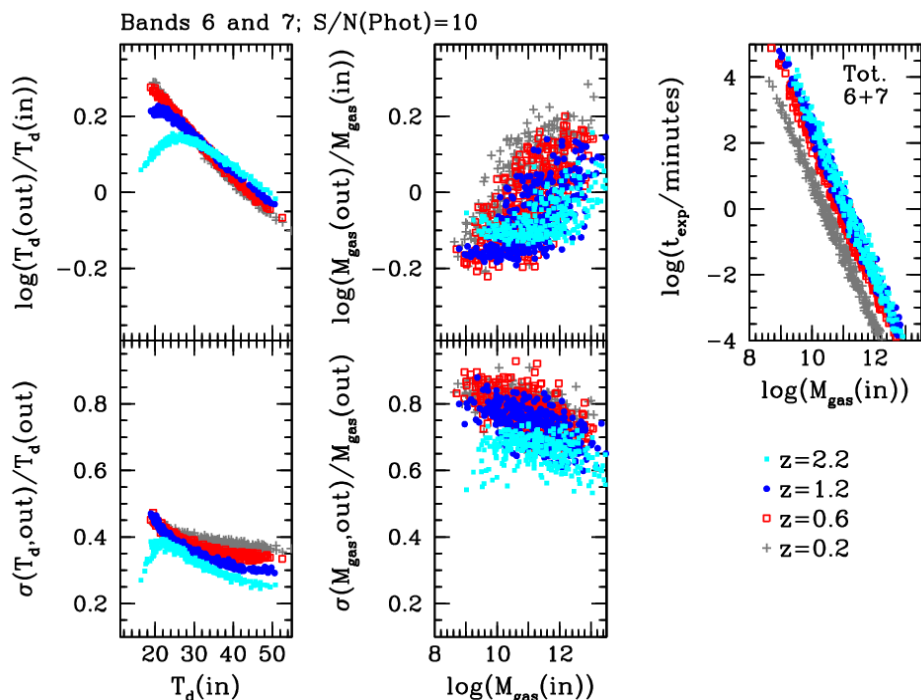


Figure 14: Performance of two band millimeter/submillimeter ALMA measurements (in bands 6 (240 GHz) and 7 (350 GHz)) for determining dust temperatures (left panels) and molecular gas mass (middle panels), as a function of input quantities for simulated galaxies on the Magnelli et al. (2014) grid, from the scaling relationships in Tables 4 and 5, and for 10σ photometry in each of the ALMA bands. The top panels show the logarithm of the ratio of the inferred quantity (dust temperature or gas mass) relative to the input quantity. The bottom panels show the 1σ fractional uncertainties in the temperature and gas mass estimates, given the flux density uncertainties of the measurements. The right panel gives the total ALMA integration time required assuming

34 antennas, for these two-band measurements, as a function of input gas mass. The color coding is for the different redshift bins as in Figures 2 & 5.

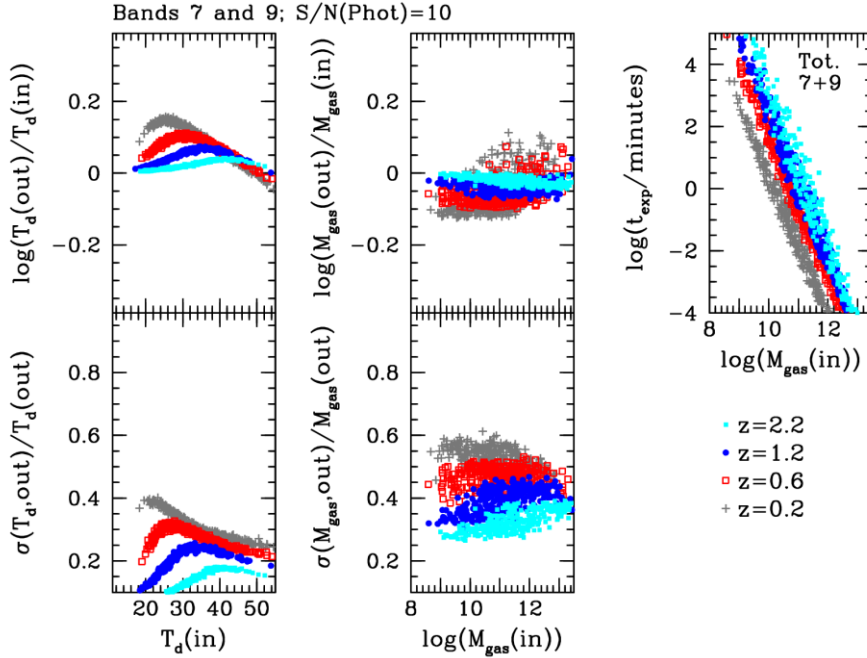


Figure 15: Performance of two band millimeter/submillimeter ALMA measurements (in bands 7 (350 GHz) and 9 (670 GHz)) for determining dust temperatures (left panels) and molecular gas mass (middle panels), as a function of input quantities for simulated galaxies on the Magnelli et al. (2014) grid, from the scaling relationships in Tables 4 and 5, and for 10σ photometry in each of the ALMA bands. The top panels show the logarithm of the ratio of the inferred quantity (dust temperature or gas mass) relative to the input quantity. The bottom panels show the 1σ fractional uncertainties in the temperature and gas mass estimates, given the flux density uncertainties of the measurements. The right panel gives the total ALMA integration time required for these

two-band measurements, as a function of input gas mass. The color coding is for the different redshift bins as in Figures 2 & 5.

Table 1. CO sample

redshift range	N (± 0.6 dex of ms)	N above 0.6 dex ms	N below 0.6 dex ms
0 - 0.05 $\langle \rangle = 0.033$ N=296	193	54	49 (including 1 stack)
0.05 - 0.45 $\langle \rangle = 0.1$ N=55	12	43	0
0.45 - 0.85 $\langle \rangle = 0.67$ N=48	30	18	0
0.85 - 1.2 $\langle \rangle = 1.1$ N=32	26	5	1
1.2 - 1.75 $\langle \rangle = 1.4$ N=28	25	3	0
1.75 - 4.1 $\langle \rangle = 2.3$ N=41	28	11	2
total 500	314	134	52

Table 2. dust sample

mean redshift	N (± 0.6 dex of ms)	N above 0.6 ms	N below 0.6 ms
0.1 N=30	26	3	1
0.35 N=87	61	23	3
0.65 N=83	56	27	0
1 N=191	137	52	2
1.45 N=88	68	21	0
2 N=33	22	10	1
total N= 512	369	136	7

Table 3. Parameters of power law fitting function for t_{depl} -scaling relations

	a_{f1}^a	ξ_{f1}^a	ξ_{g1}^a	ξ_{h1}^a
CO-data: binned	-0.04 (0.01)	-0.165 (0.04)	-0.46 (0.03)	-0.002 (0.03)
global	-0.042 (0.01)	-0.13 (0.05)	-0.45 (0.03)	---
global, z=0 down-weighted ^b	-0.02 (0.024)	-0.16 (0.07)	-0.48 (0.03)	---
dust-data: binned	0.335 (0.06)	-0.77 (0.19)	-0.59 (0.05)	-0.01 (0.03)
global	0.31 (0.13)	-0.67 (0.45)	-0.60 (0.1)	-0.01 (0.1)
average: binned	+0.07 (0.1)	-0.36 (0.1)	-0.51 (0.03)	-0.01 (0.02)
global^c	+0.08 (0.1)	-0.31 (0.05)	-0.5 (0.02)	0.003 (0.02)
global (Lilly) ^d	+0.01 (0.02)	-0.30 (0.05)	-0.5 (0.02)	-0.15 (0.02)
global ($g_1(sSFR)$) ^e	-0.46 (0.02)	1.18 (0.06)	-0.5 (0.02)	-0.197 (0.02)

$$\begin{aligned}
 \log(t_{\text{depl}}(z, sSFR, M_*) |_{\alpha=\alpha_{MW}}) &= \\
 &\log(f_1(z) |_{sSFR=sSFR(ms, z, M_*)}) \\
 &+ \log(g_1(sSFR / sSFR(ms, z, M_*))) \\
 &+ \log(h_1(M_*)) \\
 &= a_{f1} + \xi_{f1} \times \log(1+z) + \xi_{g1} \times \log(sSFR / sSFR(ms, z, M_*)) + \xi_{h1} \times (\log(M_*) - 10.5)
 \end{aligned}$$

^a in each of the columns the first fit value given comes from the ‘parameter separated, binned’ method discussed in sections 3.1 and 3.2 (6 redshift bins, first fitting the zero points of the $\log(sSFR/sSFR(ms, z, M_*))$ dependence with an assumed slope of -0.46 (CO) and -0.59 (dust), then subtracting the zero points and fitting the $\log(sSFR/sSFR(ms, z, M_*))$ slope for all data, then subtracting these fits values to finally fit the $\log M_*$ dependence. All fits were made with power law functions. The second fit value comes from a direct,

global fit to all data (not binned) in the 3-space, $\log(1+z)$, $\log(sSFR/sSFR(ms,z,M_*))$, $\log t_{depl}$, and assuming no dependence on stellar mass (section 3.2.1), again with a linear fitting function. The values in parentheses are the 1σ fit uncertainties. In the case of the global fits these were determined by perturbing the original $\log(sSFR/sSFR(ms,z,M_*))$ and $\log t_{depl}$ measurements repeatedly with the ± 0.2 dex errors and repeating the global fits.

^b to explore the influence of the unequal numbers of points (~ 300 $z \leq 0.05$ data from COLDGASS and GOALS) we down-weighted each of these by 2.7 to give all the z -bins approximately the same weight.

^c For the global combined CO+dust fit we first added 0.11 dex to all CO depletion time values, and likewise subtracted 0.11 dex for all dust depletion times before carrying out the global fit, in order to bring the two data sets to the same zero-point.

^d For this row we carried out a combined CO and dust global fit (1012 data points) we proceeded as above in ^b but now employed the Lilly et al. (2013) prescription for the main-sequence, $sSFR(ms,z,M_*) = 0.117 (\text{Gyr}^{-1}) \times (M_*/3.16 \times 10^{10} M_\odot)^{-0.1} \times (1+z)^3$ for $z < 2$, and $sSFR(ms,z,M_*) = 0.5 (\text{Gyr}^{-1}) \times (M_*/3.16 \times 10^{10} M_\odot)^{-0.1} \times (1+z)^{1.667}$ for $z \geq 2$, instead of the one by Whitaker et al. (2012, eq.1). The Lilly et al. (2013) fitting function is a simple power law in stellar mass (without curvature, as in Whitaker et al.). It captures the actual location of the SFGs in the stellar mass- $sSFR$ plane quite well at $\log M_* = 9.5$ to 10.5 and $z = 0 = 2.5$ but the more massive galaxies then systematically lie below the Lilly et al. fit.

^e For this row we again combined the CO and dust data in a global fit and assumed that g_l depends only on $sSFR$ (Gyr^{-1}), without referring to the main sequence.

Table 4. parameters of power law fitting function for M_{molgas}/M_* -scaling relations

	$a_{f_2}^a$	$\xi_{f_2}^a$	$\xi_{g_2}^a$	$\xi_{h_2}^a$
CO-data	-1.23 (0.01)	+2.71 (0.09)	+0.51 (0.03)	-0.35 (0.03)
global	-1.14 (0.012)	+2.78 (0.05)	+0.53 (0.02)	-0.35 (0.02)
dust-data	-0.87 (0.06)	+2.26 (0.24)	+0.51 (0.05)	-0.41 (0.03)
global	-0.94 (0.03)	+2.64(0.45)	+0.41 (0.1)	-0.54 (0.1)
average	-1.1 (0.05)	+2.6 (0.1)	+0.51 (0.03)	-0.38 (0.03)
global^b	-1.11 (0.02)	+2.77 (0.05)	+0.50 (0.03)	-0.44 (0.03)
global (Lilly) ^c	-0.98 (0.02)	+2.65 (0.05)	+0.50 (0.03)	-0.25 (0.03)
global (sSFR) ^d	-0.51 (0.02)	+1.18 (0.06)	+0.50 (0.03)	-0.198 (0.03)

$$\begin{aligned}
 \log(M_{\text{molgas}} / M_*(z, sSFR, M_*) |_{\alpha=\alpha_{MW}}) = & \\
 & \log(f_2(z) |_{sSFR=sSFR(ms, z, M_*)}) \\
 & + \log(g_2(sSFR / sSFR(ms, z, M_*))) \\
 & + \log(h_2(M_*)) \\
 = & a_{f_2} + \xi_{f_2} \times \log(1+z) + \xi_{g_2} \times \log(sSFR / sSFR(ms, z, M_*)) + \xi_{h_2} \times (\log(M_*) - 10.77)
 \end{aligned}$$

^a in each of the columns the first fit value given comes from the ‘parameter separated, binned’ method discussed in sections 3.1 and 3.2 (6 redshift bins, first fitting the zero points of the $\log(sSFR/sSFR(ms, z, M_*))$ dependence with an assumed slope of 2.7 (CO) and -2.6 (dust), then subtracting the zero points and fitting the $\log(sSFR/sSFR(ms, z, M_*))$)

slope for all data, then subtracting these fits values to finally fit the $\log M_*$ dependence. All fits were made with power law functions. The second fit value comes from a direct, global fit to all data (not binned) in the 4-space, $\log(I+z)$, $\log(sSFR/sSFR(ms,z,M_*))$, $\log(M_*)$, $\log(M_{gas}/M_*)$, again with a linear fitting function. The values in parentheses are the 1σ fit uncertainties. In the case of the global fits these were determined by perturbing the original $\log(sSFR/sSFR(ms,z,M_*))$ and $\log(M_{gas}/M_*)$, measurements repeatedly with the ± 0.2 dex errors, and the $\log(M_*)$ values with ± 0.15 dex errors, and repeating the global fits.

^b For the global combined CO+dust fit (1012 data points) we first added 0.11 dex to all CO M_{gas}/M_* values, and likewise subtracted 0.11 dex for all dust M_{gas}/M_* values before carrying out the global fit, in order to bring the two data sets to the same zero-point.

^c For this row we carried out a combined CO and dust global fit (1012 data points) we proceeded as above in ^b but now employed the Lilly et al. (2013) prescription for the main-sequence, $sSFR(ms,z,M_*)=0.117 (Gyr^{-1}) \times (M_*/3.16 \times 10^{10} M_\odot)^{-0.1} \times (1+z)^3$ for $z < 2$, and $sSFR(ms,z,M_*)=0.5 (Gyr^{-1}) \times (M_*/3.16 \times 10^{10} M_\odot)^{-0.1} \times (1+z)^{1.667}$ for $z \geq 2$, instead of the one by Whitaker et al. (2012, eq.1). The Lilly et al. (2013) fitting function is a simple power law in stellar mass (without curvature, as in Whitaker et al.). It captures the actual location of the SFGs in the stellar mass- sSFR plane quite well at $\log M_* = 9.5$ to 10.5 and $z = 0 = 2.5$ but the more massive galaxies then systematically lie below the Lilly et al. fit.

^d For this row we again combined the CO and dust data in a global fit and assumed that g_2 is only a function of sSFR (Gyr^{-1}), without referring to the main sequence.

Table 5. Parameters of power law fitting function for T_{dust} -scaling relations

	a_{f3}	ξ_{f3}	ξ_{g3}	ξ_{h3}
dust-data	1.4296 (0.006)	+0.105 (0.02)	+0.086 (0.003)	-0.012 (0.003)

$$\begin{aligned}
 \log(T_{\text{dust}}) &= \log(f_3(z) |_{s\text{SFR}=s\text{SFR}(ms,z)}) + \log(g_3(s\text{SFR} / s\text{SFR}(ms, z))) + \log(h_3(M_*)) \\
 &= a_{f3} + \xi_{f3} \times \log(1+z) + \xi_{g3} \times \log(s\text{SFR} / s\text{SFR}(ms, z)) + \\
 &\quad \xi_{h3} \times (\log(M_*) - 10.7)
 \end{aligned}$$